BAR DIAGNOSTICS IN EDGE-ON SPIRAL GALAXIES. II. HYDRODYNAMICAL SIMULATIONS

E. ATHANASSOULA

Observatoire de Marseille, 2 place Le Verrier, F-13248 Marseille Cedex 4, France

AND

M. BUREAU[1]

Mount Stromlo and Siding Spring Observatories, Institute of Advanced Studies, The Australian National University,
Private Bag, Weston Creek P.O., ACT 2611, Australia

ABSTRACT

We develop diagnostics based on gas kinematics to identify the presence of a bar in an edge-on spiral galaxy and determine its orientation. We use position-velocity diagrams (PVDs) obtained by projecting edge-on two-dimensional hydrodynamical simulations of the gas flow in a barred galaxy potential. We show that when a nuclear spiral is formed, the presence of a gap in the PVDs, between the signature of the nuclear spiral and that of the outer parts of the disk, reliably indicates the presence of a bar. This gap is due to the presence of shocks and inflows in the simulations, leading to a depletion of the gas in the outer bar region. If no nuclear spiral signature is present in a PVD, only indirect arguments can be used to argue for the presence of a bar. The shape of the signature of the nuclear spiral, and to a lesser extent that of the outer bar region, allows a determination of the orientation of the bar with respect to the line of sight. The presence of dust can also help to discriminate between viewing angles on either side of the bar. Simulations covering a large fraction of parameter space constrain the bar properties and mass distribution of observed galaxies. The strongest constraint comes from the presence or absence of the signature of a nuclear spiral in the PVD.

Subject headings: galaxies: fundamental parameters — galaxies: kinematics and dynamics —
galaxies: spiral — galaxies: structure — hydrodynamics —
ISM: kinematics and dynamics

1. INTRODUCTION

The importance of bars in the structure of spiral galaxies is recognized in the Hubble sequence for the classification of galaxies (Sandage 1961). In the first paper of this series (Bureau & Athanassoula 1999, hereafter Paper I), we highlighted the difficulties involved in the identification of bars in edge-on systems. It is clear that the detection of such bars based on photometric or morphological criteria (e.g., de Carvalho & da Costa 1987; Hamabe & Wakamatsu 1989) is uncertain. Kuijken & Merrifield (1995, hereafter KM95; see also Merrifield 1996) were the first to show that the particular kinematics of barred disks could be used to identify bars in edge-on spirals. They showed that the periodic orbits in an edge-on barred galaxy produce characteristic double-peaked line-of-sight velocity distributions, which can be taken as the signature of a bar.

In Paper I, we improved on the work of KM95. We studied the signatures of individual periodic orbit *families* in the position-velocity diagrams (PVDs) of edge-on barred spirals (before combining them to model real galaxies), and examined how the PVDs depend on the viewing angle. We adopted a widely used mass model and a well-defined method to populate the periodic orbits. Our aim was to provide insight into the projected kinematical structure of barred disks, and to provide guidance in interpreting stellar and gaseous kinematical observations of edge-on spiral galaxies. We showed in Paper I that the global appearance of a PVD can be used as a diagnostic to detect the presence of a bar in an edge-on disk. The signatures of the various periodic orbit families leave gaps in the PVDs that are a

direct consequence of the nonhomogeneous distribution of orbits in a barred spiral. The signature of the x_1 periodic orbits is parallelogram-shaped and occupies all four quadrants of the PVDs, reaching very high radial velocities when the bar is seen end-on and only low velocities when the bar is seen side-on. The signature of the x_2 orbits, when present, is similar to that of the x_1 orbits, but they reach their maximum radial velocities at opposite orientations. Those features can be used to determine the viewing angle with respect to the bar in an edge-on disk. However, even if carefully chosen and populated, periodic orbits provide only an approximation to the structure and kinematics of the stars and gas in spiral galaxies. For example, a number of stars may be on irregular orbits, and shocks can develop in the gas.

In this paper (Paper II), we concentrate on developing bar diagnostics for edge-on disks using the gaseous component alone. We use the hydrodynamical simulations of Athanassoula (1992b, hereafter A92b), designed to study the gas flow and shock formation in barred spiral galaxies. Unlike Paper I, these simulations properly take into account the fact that the gas is not a collisionless medium. The shocks and inflows that develop in the simulations lead to better bar diagnostics than those of Paper I. In addition, we run simulations covering a large fraction of the parameter space likely to be occupied by real galaxies. The PVDs produced can thus be directly compared with observations not only to detect the presence of bars in edge-on spiral galaxies, but also to constrain the mass distribution of the systems observed. In particular, Bureau & Freeman (1999, hereafter BF99) have applied those diagnostics to long-slit spectroscopic observations of a large number of edge-on spiral galaxies, most of which have a boxy or peanut-shaped

[1] Now at Sterrewacht Leiden, Postbus 9513, 2300 RA Leiden, The Netherlands.

bulge, to determine the formation mechanism of these objects and study the vertical structure of bars. In Paper III (Athanassoula & Bureau 1999), using fully self-consistent three-dimensional N-body simulations, we will develop similar bar diagnostics for the stellar (collisionless) component of barred spiral galaxies.

We describe the mass model and hydrodynamical simulations used in this paper in § 2. In § 3, we study the signatures in the PVDs of the various components present in the simulations and discuss the influence of the parameters of the mass model. The effects of dust extinction are illustrated in § 4. We develop bar diagnostics for edge-on disks and discuss the limitations of our models for the interpretation of real data in § 5. We conclude in § 6 with a brief summary of our main results.

2. HYDRODYNAMICAL SIMULATIONS

For the hydrodynamical simulations, we use the flux-splitting second-order scheme of G. D. van Albada (van Albada & Roberts 1981; van Albada, van Leer, & Roberts 1982; van Albada 1985). This is the same code as used by A92b, so we will only briefly review its main properties here.

The simulations are two-dimensional and time-dependent, and the gas is treated as ideal, isothermal, and nonviscous. The simulations are not self-consistent and we do not consider the self-gravity of the gas; the flow is calculated using the potential described in Paper I (see also Athanassoula 1992a, hereafter A92a). The mass model has two axisymmetric components, a Kuzmin/Toomre disk (Kuzmin 1956; Toomre 1963) and a bulgelike spherical density distribution. They combine to yield a flat rotation curve in the outer parts of the disk. We use a homogeneous ($n = 0$) or inhomogeneous ($n = 1$) Ferrers spheroid (Ferrers 1877) as a third component representing the bar. Each model is described by four main parameters: the bar axial ratio, a/b; the quadrupole moment of the bar, Q_m (proportional to the mass of the bar); the Lagrangian radius, r_L (the radius of the Lagrange points L_1 and L_2 on the major axis of the bar, approximately inversely proportional to the bar pattern speed); and the central concentration, ρ_c. The other quantities are fixed, including the semimajor axis of the bar, $a = 5$ kpc. We refer the reader to Paper I for a more detailed description of the mass model. A92a discusses at great length its relevance to real galaxies. Suffice it to say here that the properties of the mass model are in excellent agreement with those of early-type barred spirals.

The simulations are started with a massless bar and an additional axisymmetric component of mass equal to that of the desired final bar. Mass is transferred from that component to the bar over 10^8 yr, and the simulations are run until the gas flow is roughly stationary in the frame of reference corotating with the bar (about 10 bar revolutions). A grid of 80×160 cells is used to cover a disk of 16 kpc radius, assuming bisymmetry. The inner half of the simulations are then regridded to the 80×160 grid and the simulations continued for another five bar revolutions using this increased spatial resolution (0.1×0.1 kpc^2 cell size; see van Albada & Roberts 1981). Star formation and mass loss are modeled crudely. The gas density is lowered artificially in high-density regions and gas is added uniformly over the grid. This process is governed by the equation

$$d\rho_g/dt = \alpha\rho_{g,\text{init}}^2 - \alpha\rho_g^2 , \qquad (1)$$

where ρ_g is the gas density, α is a constant (set to 0.3 $M_\odot^{-1}$ pc^2 Gyr^{-1} in most runs), and $\rho_{g,\text{init}} = 1$ $M_\odot$ pc^{-2} is the uniform initial gas density. It therefore takes about 3 Gyr for the gas to be reprocessed. There is no artificial viscosity in the code.

Our main tool in this paper will be PVDs, representing the projected density of material in the edge-on disks as a function of line-of-sight velocity and projected position along the major axis. Since we are only interested in the bar region, we use only the inner 8 kpc × 8 kpc region of the simulations, covered by the high-resolution grid. At larger radii, the motion of the gas can, to first order, be considered as circular, since the force of the bar decreases steeply with radius. Including the outer regions thus makes no difference to our PVDs.

As in Paper I, the models considered are those of A92a (see her Table 1). We will also use her units: 10^6 $M_\odot$ for masses, kpc for lengths, and km s^{-1} for velocities. It is essential to understand the orbital structure of the models to properly interpret the results of the hydrodynamical simulations. Orbital properties have been discussed in Paper I and A92a, but also in Athanassoula et al. (1983), Papayannopoulos & Petrou (1983), Teuben & Sanders (1985), and others. Here we will mainly use Paper I and A92a for comparison. We will also draw heavily on the results of A92b, who used the same set of simulations but for different purposes. She discussed in detail the gas flow and compared the results with the properties of real galaxies.

3. BAR DIAGNOSTICS

In this section, we will concentrate on understanding the PVDs of two inhomogeneous bar models that are prototypes of models with and without inner Lindblad resonances (ILRs). As suggested in A92a, we will identify the existence and position of the ILRs with the existence and extent of the x_2 periodic orbits. The two models considered are the same as in Paper I: model 001 ($n = 1$, $a/b = 2.5$, $Q_m = 4.5 \times 10^4$, $r_L = 6.0$, $\rho_c = 2.4 \times 10^4$) and model 086 ($n = 1$, $a/b = 5.0$, $Q_m = 4.5 \times 10^4$, $r_L = 6.0$, $\rho_c = 2.4 \times 10^4$). We will then extend our results to other models and analyze how the properties of the PVDs vary as the parameters of the mass model are changed.

3.1. Model 001 (ILRs)

Figure 1 shows PVDs for model 001, which has ILRs. The figure shows, for the inner half of the simulation, the face-on surface density of the gas and PVDs obtained projecting the simulation edge-on and using various viewing angles with respect to the bar. Unlike the models of Paper I, which are symmetric around both the minor and major axes of the bar, the present simulations are bisymmetric, so we need to cover a viewing angle range of 180°. The viewing angle ψ is defined to be 0° for a line of sight parallel to the major axis of the bar and 90° for a line of sight perpendicular to it, increasing counterclockwise in the surface density plots.

A92b showed convincingly that the two strong parallel narrow segments present in the surface density plot of Figure 1 represent offset shocks on the leading sides of the bar, displaying strong density enhancements and sharp velocity gradients. They can be identified with the dust lanes observed in barred spiral galaxies. The structures seen at the
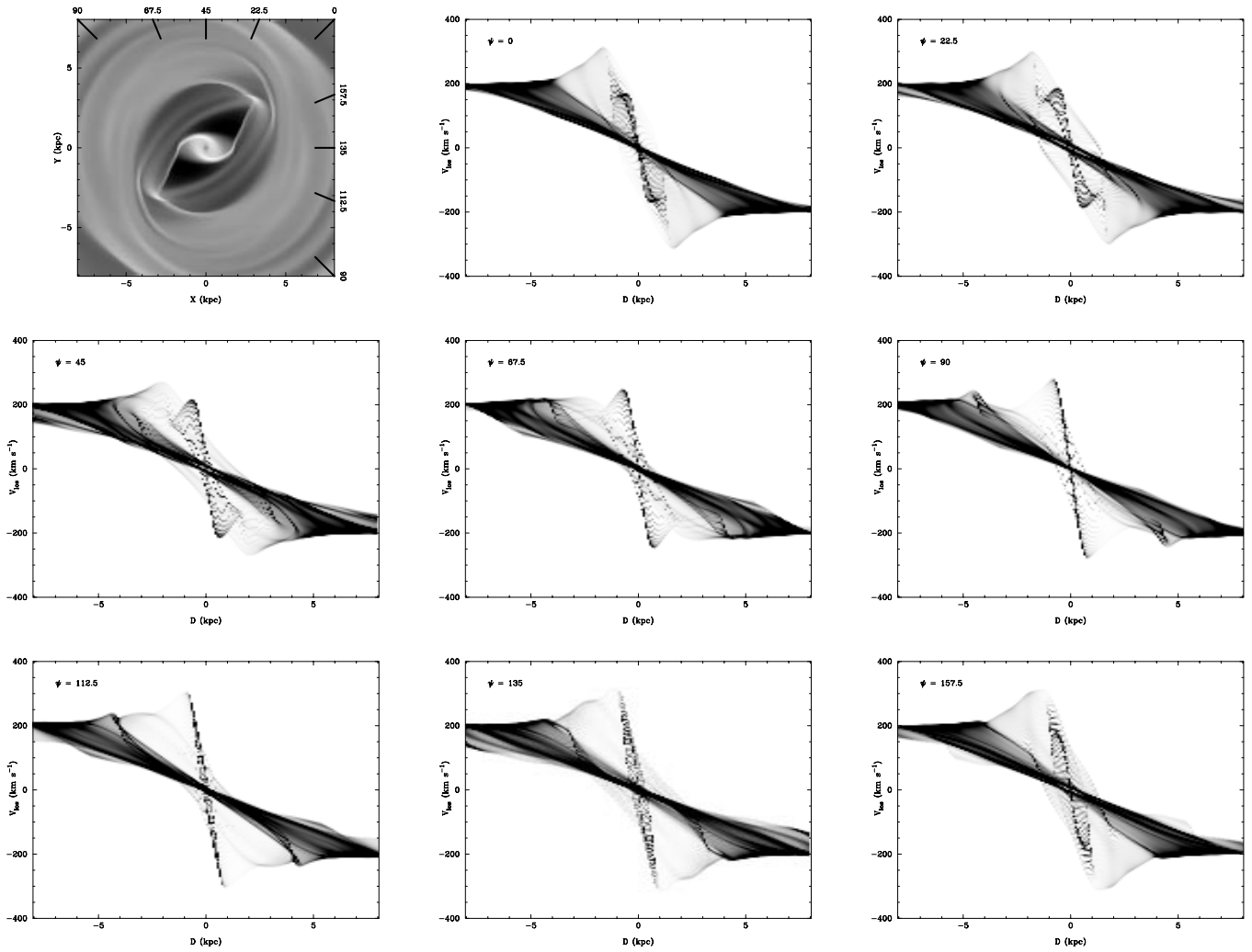
Fig. 1.—Gas distribution and position-velocity diagrams of model 001, with $n = 1$, $a/b = 2.5$, $r_L = 6.0$, $\rho_c = 2.4 \times 10^4$, and $Q_m = 4.5 \times 10^4$. The upper left plot shows the face-on logarithmic gas surface density of the simulation. We use logarithmic values (in this plot alone) because the dynamic range of the gas surface density is high. Dark shading denotes low-density regions. The bar is at 45° to the horizontal, has a semimajor axis length of 5 kpc, and is rotating clockwise. The other plots show position-velocity diagrams (projected density of material as a function of line-of-sight velocity and projected position along the major axis) of the gas when the simulation is viewed edge-on. For those plots, dark shading denotes high-density regions. The angle between the line of sight and the bar is indicated in the top left corner of each diagram, a viewing angle of $\psi = 0°$ indicating that the bar is seen end-on (line of sight parallel to the bar) and a viewing angle of $\psi = 90°$ indicating that the bar is seen side-on (line of sight perpendicular to the bar). The viewing angle is illustrated in the surface density plot and increases counterclockwise.

ends of the bar and perpendicular to it are also shocks. In the inner bar region is a very intense two-arm nuclear spiral, connecting with the offset shocks. There is little gas in the barred region outside the nuclear spiral, which we will hereafter refer to as the outer bar region. Beyond the bar the surface density is almost featureless; only a few spiral arms are seen. A92b showed that, in the outer bar region, the streamlines have roughly the shape and orientation of the x_1 periodic orbits. As one moves inward, the streamlines change gradually to the shape and orientation corresponding to the x_2 periodic orbits. This flow pattern leads to the offset shocks and results in an inflow of gas toward the nuclear region. It accounts for the gas distribution in the bar: low densities in the outer bar region and high densities in the center. The velocities are small (in the reference frame corotating with the bar) around the Lagrange points on the minor axis of the bar, and the flow is close to circular outside the bar region.

The PVDs in Figure 1 show the existence of three distinct regions: an inner region, corresponding to the signature of the nuclear spiral; an intermediate region, corresponding to the signature of the outer parts of the bar; and an external region, corresponding to the signature of the disk outside the bar. It is important to notice how low the density of the intermediate region is, compared to that of the other two regions. This is not surprising, since, as mentioned in A92b and above, most of the bar region has a very low gas density, with the exception of the central part (the nuclear spiral) and the two shock loci. This will form the basis of the bar diagnostics we develop later on. Let us now examine each of the three regions separately, by keeping only the gas in the targeted region (and masking out the gas in the other regions) when calculating the PVDs.

Figure 2 shows the surface density and PVDs of model 001 when considering the low-density outer bar region only. Because the high-density regions have been masked out,
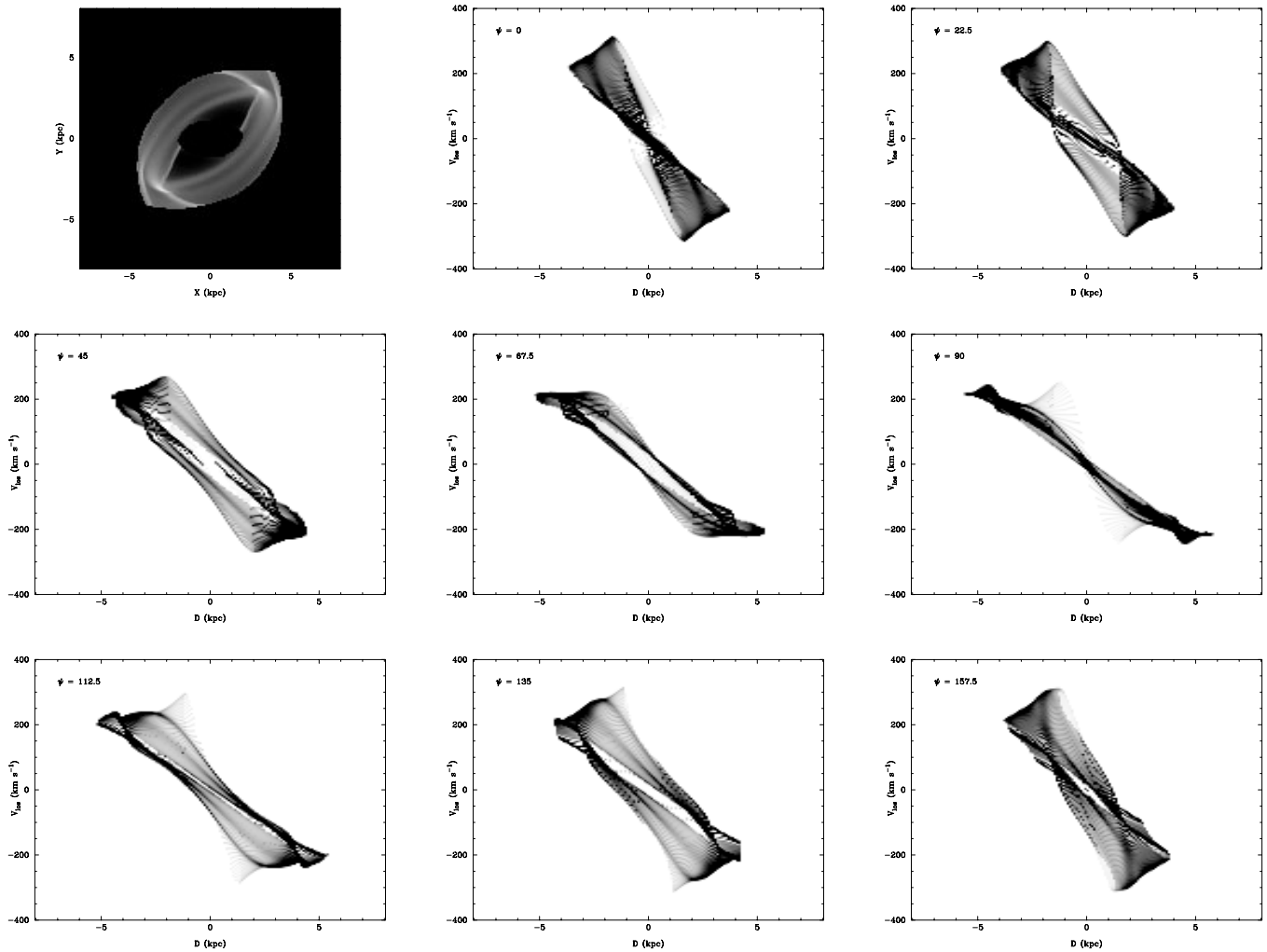
FIG. 2.—Same as Fig. 1, but for the low-density outer bar region of model 001 only

and because we are looking only at relatively low density regions, we see much more structure in the PVDs of Figure 2 than in the corresponding sections of the PVDs of Figure 1.

When compared with Figure 4 of Paper I, Figure 2 shows at first glance many similarities, but when scrutinized closer also a number of differences. This is to be expected since the gas streamlines in that region follow loosely, but far from exactly, the shape and orientation of the x_1 orbits, which are elongated parallel to the bar.

The parallelogram-shaped signature of the x_1 orbits in Figure 4 of Paper I is observed again here, and the "forbidden" quadrants are again populated. This is due to the fact that both the x_1 orbits and the streamlines in the outer bar region are not circular but elongated. In the gas, however, the parallelogram shape is also present for $\psi = 0°$, while for this viewing angle the PVD of the x_1 orbits showed a bow-shaped feature. This is because, unlike the x_1 orbits, the streamlines do not have their major axes parallel to that of the bar, but rather at an angle about 20° to it (see A92b). In addition, at $\psi = 90°$, the x_1 orbits show a near-linear PVD, while the gas shows an additional faint bow-shaped feature reaching high velocities near the center. Masking out a larger fraction of the simulation (not shown), it is possible to show that this extra feature arises from the

very low density areas just inside the offset shocks, close to the major axis of the bar. In this section of the bar, the flow differs substantially from the behavior of the x_1 periodic orbits. The elongated "hole" in the center of the PVDs at intermediate viewing angles is present in both sets of PVDs, and is due to the ways in which the x_1 family was terminated and the gas density masked out. In both cases this causes an absence (or low density) of quasi-circular streamlines near the end of the bar. In the hydrodynamical simulation, there is also a reduced degree of symmetry with respect to viewing angles of 0° or 90°, in particular for the angles 67°.5 and 112°.5. These are, of course, identical in the PVDs of Paper I. This is because the gas flow is bisymmetric, as opposed to being symmetric with respect to both the minor and major axes of the bar, as are the x_1 orbits (see Fig. 2 of A92b).

In Figure 2, we see that the radial velocities are maximum (compared to the circular velocity) for lines of sight almost parallel to the bar (highest values for $\psi = 0°$ and 157°.5), and decrease as ψ increases, to reach a minimum when the line of sight is roughly along the bar minor axis (lowest values for $\psi = 90°$ and 67°.5). The same behavior was seen for the PVDs of the x_1 orbits (Paper I), but with a slight shift of the viewing angle, so that the maximum and minimum occurred at exactly 0° and 90°, respectively. This was to be
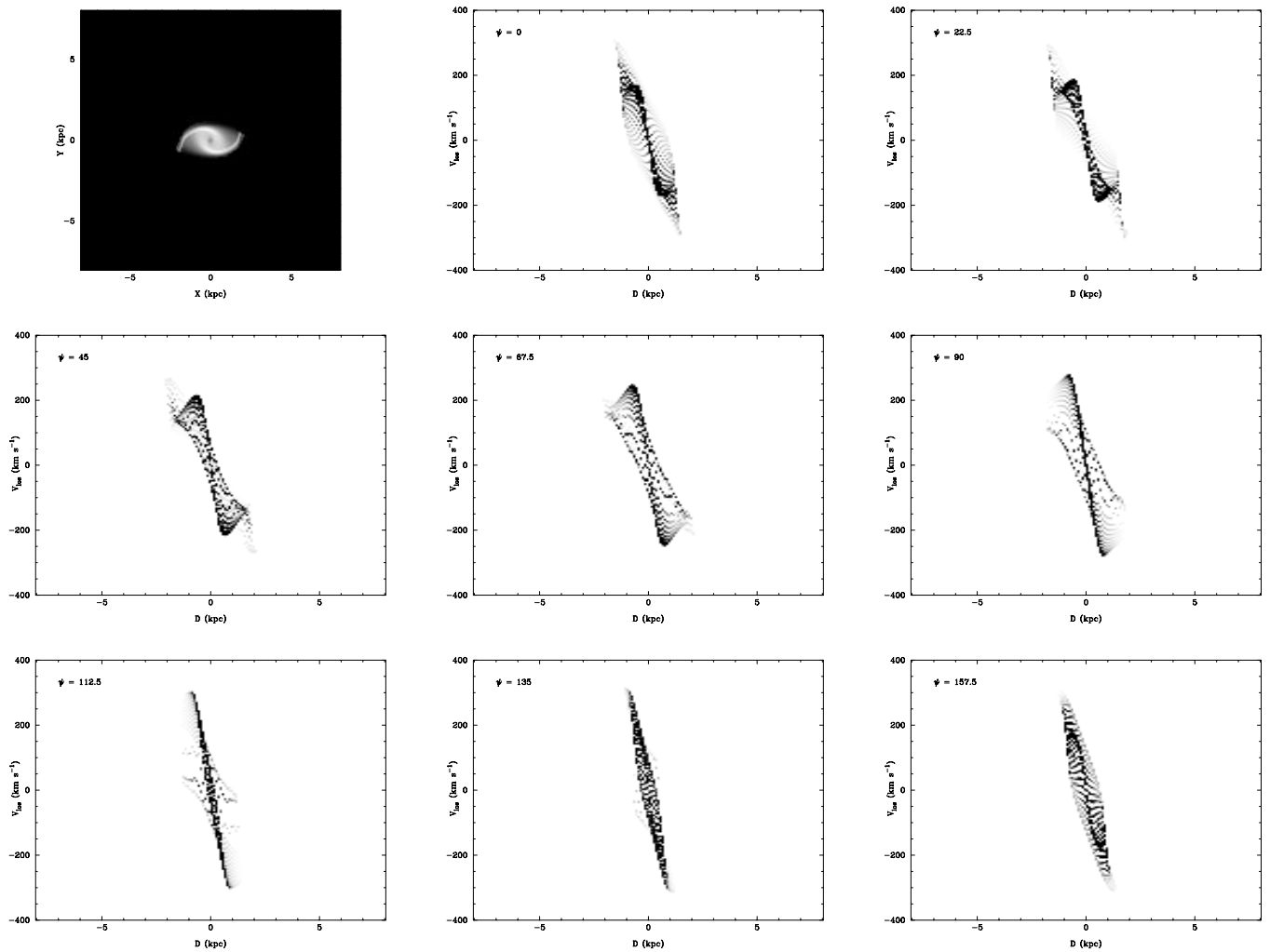
FIG. 3.—Same as Fig. 1, but for the high-density nuclear spiral region of model 001 only

expected, since, like the x_1 orbits, the streamlines in the outer bar region are elongated parallel to it (with a small offset). Similarly, the position at which the maximum occurs moves out as the viewing angle increases from $\psi = 0°$ to $\psi = 90°$. This was also found for the x_1 orbits (Paper I), where it was explained by considering the trace of an elongated orbit in a PVD as a function of viewing angle and distance from the center. The explanation is analogous here. However, in the hydrodynamical simulation, the maxima generally occur at a larger distance from the center than in the periodic orbits approach (this is easily seen by comparing Fig. 2 to Fig. 4 of Paper I). This is due to the fact that the x_1-like flow does not extend up to the center of the simulated galaxy (contrary to the x_1 orbits in Paper I), but is superseded by an x_2-like flow at a certain radius. For example, the nuclear spiral (which has an x_2-like behavior) extends about 1.6 kpc on the minor axis of the bar, which is the projected distance at which the envelope of the signature of the outer bar region in the PVD for $\psi = 0°$ drops abruptly.

To see which features of the gas distribution contribute to the PVDs, we have repeated the blanking exercise, this time masking out all areas except either the shock loci along the leading sides of the bar or the density enhancements near the ends of the bar major axis (not shown). The gas in the

shock loci does not contribute any outstanding features to the PVDs, mainly because the amount of gas integrated along most lines of sight is small, the features being very narrow. At $\psi = 22°.5$, when the line of sight is nearly parallel to the shock loci, they contribute the two straight and parallel segments separating the intense and faint regions of the PVD just inside $D = \pm 2$. The high-density enhancements near the ends of the bar major axis contribute the very strong linear segment going through the center of the PVDs at $\psi = 0°$ and $22°.5$. For these angles, they are seen roughly as segments of circles. For viewing angles near $90°$, they give rise to the undulating parts of the PVDs at large radius.

We can repeat the masking process to keep only the region of the simulation containing the nuclear spiral, as shown in Figure 3. Comparing the PVDs thus obtained with those of the x_2 family of periodic orbits (Fig. 5 of Paper I), we again find many similarities, but also some differences. In both cases, we see either an inverted S-shaped feature or a nearly straight segment passing through the center of the PVDs. We refer the reader to Paper I for a discussion and explanation of these shapes. Greater similarity is found, however, if we compare PVDs at viewing angles differing by $\approx 20°$, e.g., comparing the gaseous PVD at $\psi = 112°.5$ to the orbital one at $\psi = 90°$.
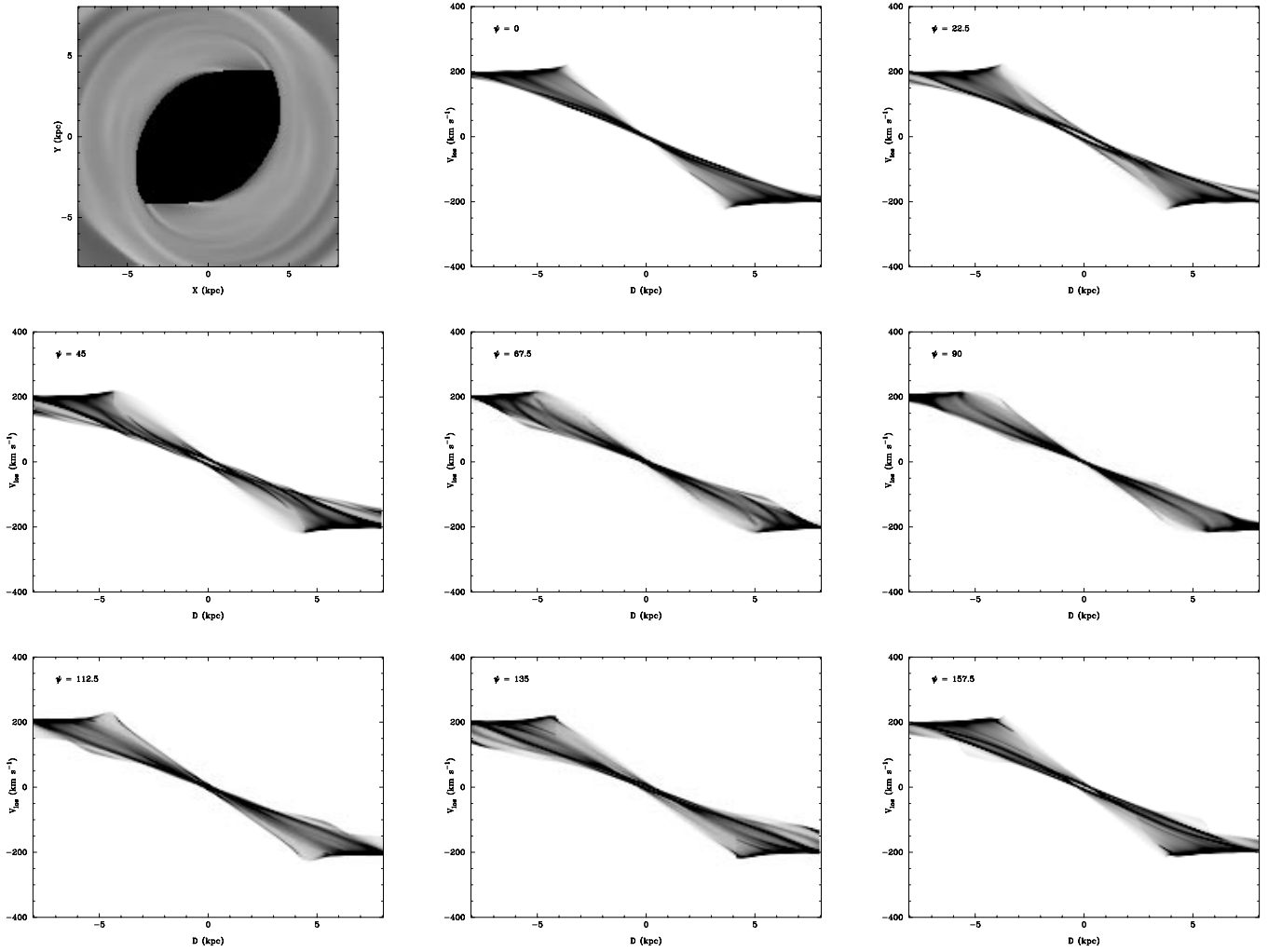
FIG. 4.—Same as Fig. 1, but for the high-density outer regions of model 001 only

This offset seems to corresponds to an offset of the nuclear spiral with respect to the minor axis of the bar (and to the offset of the straight shocks with respect to the major axis; see A92b), although this is hard to measure in the surface density plot. In addition, the PVDs of the nuclear spiral are more asymmetric with respect to the viewing angles 0° or 90° than the PVDs of the outer bar region (e.g., comparing the PVDs at $\psi = 22°\!.5$ and $\psi = -22°\!.5 = 157°\!.5$). This is due to the weaker symmetry of the nuclear spiral.

Because the streamlines in the central region are elongated roughly perpendicular to the bar, like the x_2 orbits, higher radial velocities (compared to the circular velocity) are reached when the bar is seen side-on than when the bar is seen end-on. Considering the maximum velocity of the PVDs as a function of the viewing angle, we find that it is highest for $\psi = 112°\!.5$ and 135° and lowest for $\psi = 0°$ and 22°.5. The "hole" in the parallelogram-shaped signature of the x_2 orbits (see Fig. 5 of Paper I) has completely disappeared in the hydrodynamical simulation, because the x_2-like flow persists past the inner ILR and the flow becomes almost circular in the very center.

Figure 4 isolates the signature of the outer parts of the simulation in the PVDs. Because the influence of the bar decreases rapidly with radius, the flow outside the bar is close to circular. A perfectly circular orbit would yield an

identical inclined straight line passing through the origin in all PVDs. The structure seen here can thus be thought of as a succession of near-circular orbits of increasing radii, yielding the "bow-tie" signature observed. The "hole" seen in the center of the PVDs at certain viewing angles (e.g., $\psi = 45°$) is again due to the fact that the orbits are not perfectly circular. The strong almost solid-body features forming loop-like structures near the upper and lower limits of the envelope of the signature are due to tightly wound spiral arms in the outer disk.

3.2. Model 086 (No ILRs)

Figure 5 shows the face-on surface density distribution of model 086, which has no ILRs (or, equivalently, has no x_2 periodic orbits), and the PVDs obtained using an edge-on projection. The main difference with the density distribution of model 001 is the absence of any significant nuclear spiral. The strong straight and narrow features in the center of the bar are centered shock loci, caused by the high curvature of the streamlines near the major axis of the bar (see Fig. 4 in A92b). Similarly, the x_1 orbits in this model have high curvatures or loops near their major axes (A92a). The shock loci do not curve near the center because no streamline perpendicular to the bar exists; there is no x_2 periodic orbit in this model. The shocks, however, still drive an
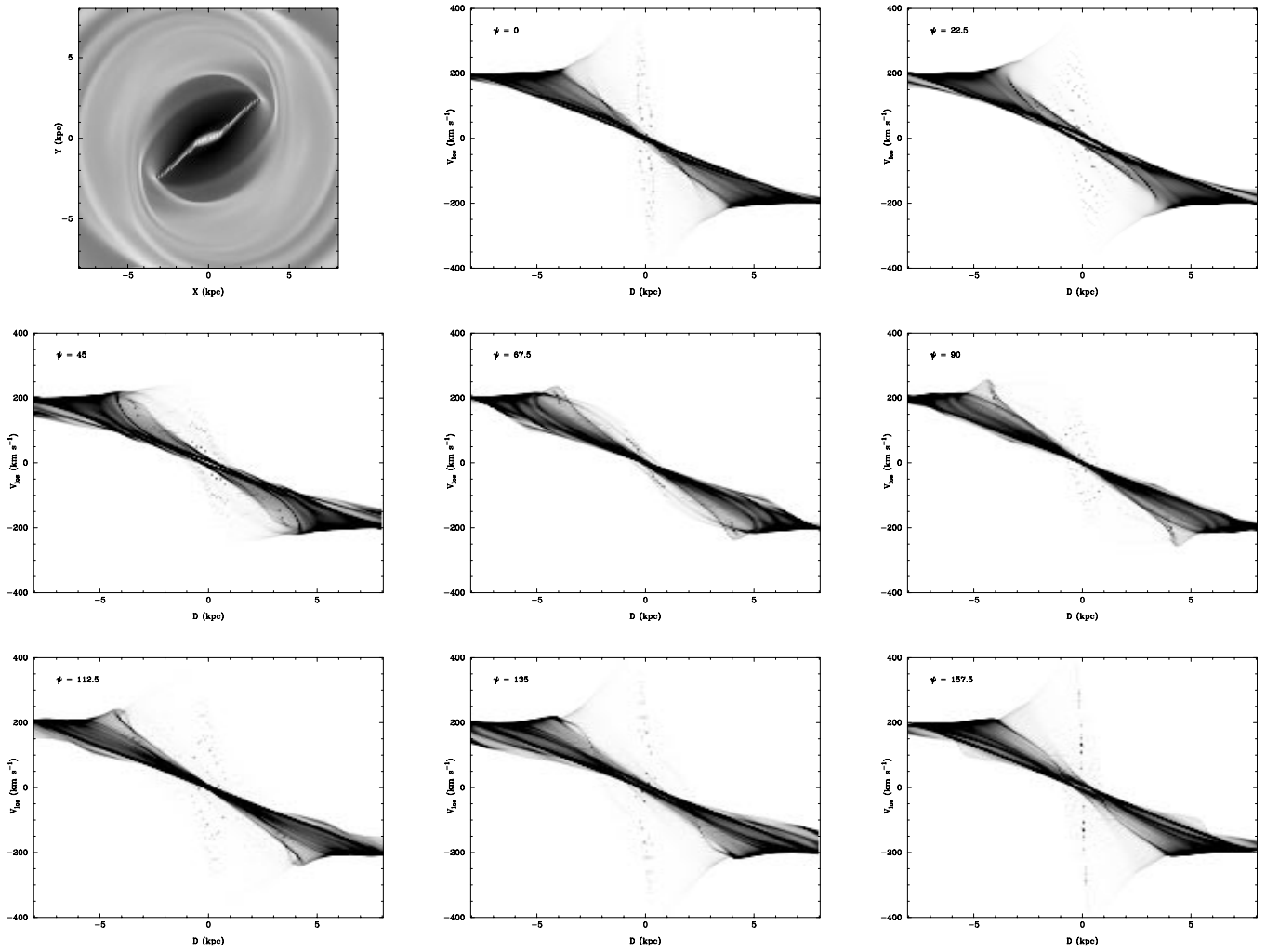
FIG. 5.—Same as Fig. 1, but for model 086, with $n = 1$, $a/b = 5.0$, $r_L = 6.0$, $\rho_c = 2.4 \times 10^4$, and $Q_m = 4.5 \times 10^4$

inflow of gas, resulting in the *entire* bar region being gas depleted. As expected, the region outside the bar is almost unaffected by the change in the bar axial ratio compared to model 001.

The PVDs for model 086 reflect all of the above properties. In particular, they lack the central feature associated with the nuclear spiral in model 001, and the signature of the bar region is very faint (Fig. 5 should be contrasted with Fig. 1). Because of the absence of an x_2-like flow in the center of the simulation, the x_1-like flow extends all the way to the center. In good agreement with the behavior of the periodic orbits (see Paper I or A92a), the streamlines are much more eccentric than those of model 001. The parallelogram-shaped envelope of the signature of the bar region in the PVDs therefore reaches even more extreme radial velocities (compared to the circular velocity) than in model 001, and the rising part of the envelope extends almost all the way to the center for viewing angles close to 0° (see also Fig. 9 in Paper I). When the bar is seen close to end-on, radial velocities more than twice those in the outer parts are reached. These velocities decrease rapidly as the viewing angle approaches $\psi = 90°$. Unfortunately, the signature of the bar region in the PVDs is very faint, because of the strong inflow gas. As in the case of model 001, the regions outside the bar lead to a strong almost solid-body component in all PVDs.

3.3. *Other Models*

In this section, we will analyze sequences of simulations corresponding to the ranges along the axes of parameter space likely to be occupied by real galaxies. We hope thereby to further our understanding of the PVDs of edge-on barred spiral galaxies, and to be able to extend the bar diagnostics that we will develop. We also wish to develop criteria allowing us to constrain the bar properties and mass distribution of edge-on systems. To achieve this, we will concentrate on understanding the PVDs of the gas flow within the barred region of the simulations, and for that purpose we will make extensive use of the results of A92a and A92b. In particular, A92b showed that nuclear spirals occur in models with an extended x_2 family of periodic orbits and lead to offset shocks, while centered shocks occur in models with no or shortly extended x_2 orbits. She also showed that x_1 periodic orbits with a high curvature near the major axis of the bar are essential to the formation of shocks, and that such shocks lead to an inflow of gas toward the central regions of the simulations, depleting the outer (or entire) bar regions.

Figure 6 shows a sequence of simulations with varying bar axial ratios a/b (the other parameters are kept fixed at those of model 001). The figure shows, for each simulation, the face-on surface density distribution and the velocity
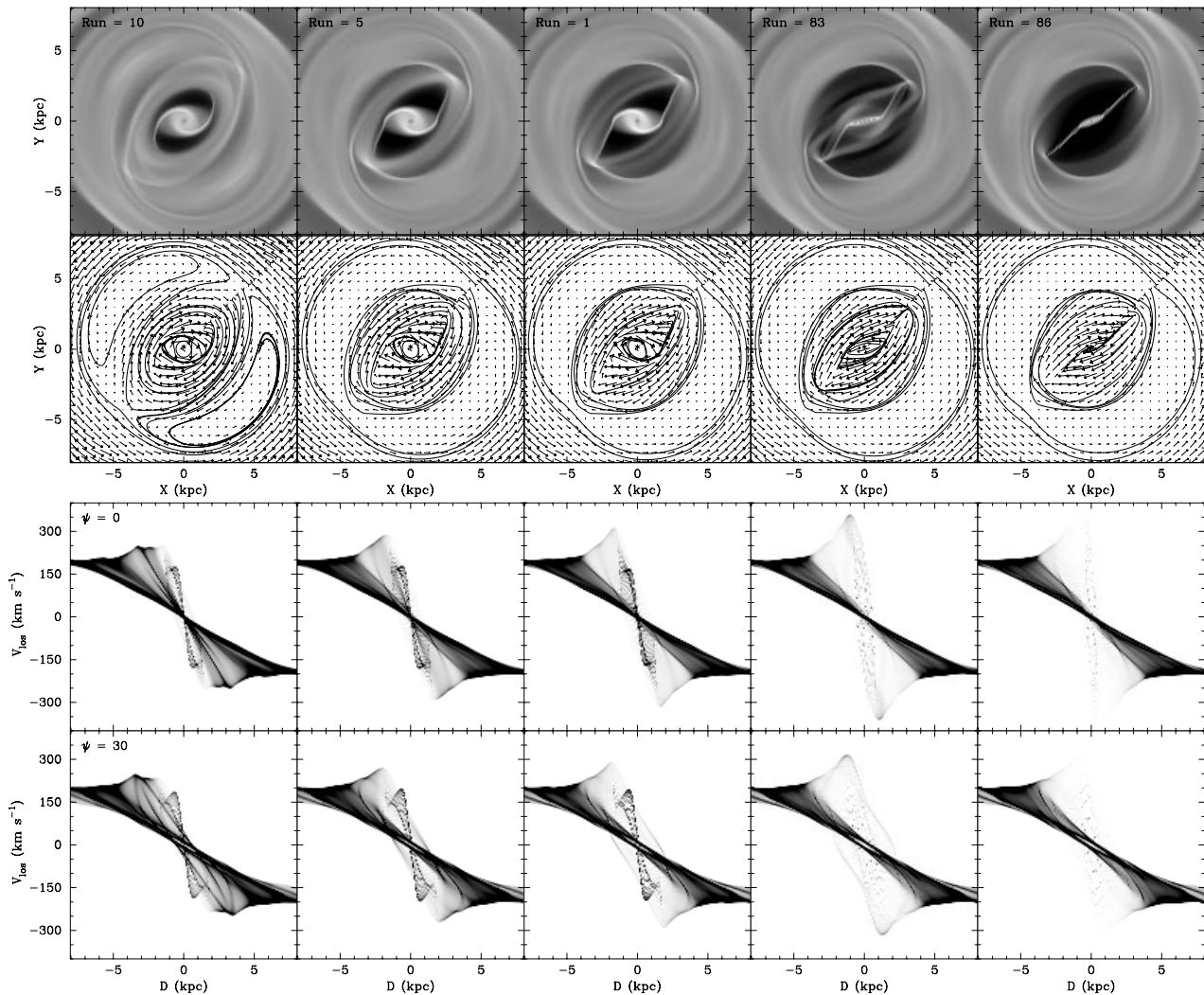
FIG. 6.—Gas distribution and position-velocity diagrams for a sequence of models of increasing bar axial ratio a/b. From left to right, the models are 010, 005, 001, 083, and 086, with $a/b =$ 1.5, 2.0, 2.5, 3.0, and 5.0, respectively. The other parameters of the models are kept fixed at those of model 001: $n = 1$, $r_L = 6.0$, $\rho_c = 2.4 \times 10^4$, and $Q_m = 4.5 \times 10^4$. The first row of plots shows the face-on logarithmic gas surface density of the simulations. We use logarithmic values (in these plots alone) because the dynamic range of the gas surface density is high. Dark shading denotes low-density regions. The bar is at 45° to the horizontal, has a semimajor axis length of 5 kpc, and is rotating clockwise. The second row of plots shows velocity vectors and gas streamlines in the frame of reference corotating with the bar. The bottom six panels show position-velocity diagrams (projected density of material as a function of line-of-sight velocity and projected position along the major axis) of the gas when the simulations are viewed edge-on. For those plots, dark shading denotes high-density regions. The angle between the line of sight and the bar is indicated in the top left corner of the first diagram of each row, a viewing angle of $\psi = 0°$ indicating that the bar is seen end-on (line of sight parallel to the bar), and a viewing angle of $\psi = 90°$ indicating that the bar is seen side-on (line of sight perpendicular to the bar). The viewing angle increases counterclockwise in the surface density plots.

field (with a few streamlines) in the frame of reference corotating with the bar. It also shows the PVDs obtained for various viewing angles with respect to the bar when the simulation is viewed edge-on. To limit the size of the figure, we show a slightly reduced number of viewing angles compared to Figures 1–5.

For small bar axial ratios, when the shocks are short and curved, the outer bar region is not strongly gas depleted and its signature is easily visible in the PVDs. As we consider simulations with increasingly high bar axial ratios, the density of the region of the PVDs corresponding to the outer bar region drops considerably. It reaches its lowest values for the highest bar axial ratio considered ($a/b = 5.0$), for which the shock loci are straight and close to the bar major axis. The envelope of the signature of the outer bar region in the PVDs becomes more extreme as the bar axial ratio is increased: the maximum radial velocities reached

for small viewing angles increase and the positions of the maxima get closer to the center. These behaviors are quasi-linear, and the opposite is true for large viewing angles. For example, at $\psi = 0°$, the maximum velocity of the outer bar region is about 250 for $a/b = 1.5$, 360 for $a/b = 3.0$, and 430 for $a/b = 5.0$. At $\psi = 90°$, the opposite is observed, with maximum velocities of about 225 and 215, respectively. This is easily understood, because as the bar axial ratio increases, the eccentricity of the streamlines in the outer bar region (and that of the x_1 orbits; see A92a) also increases, leading to higher velocities along the line of sight when the bar is seen end-on and lower velocities when the bar is seen side-on. The most important effect of an increase of the bar axial ratio is the disappearance of the nuclear spiral for axial ratios $a/b \gtrsim 2.7$. Because the nuclear spiral is associated with an x_2-like flow, and because the range of radii occupied by the x_2 orbits decreases rapidly as the bar axial
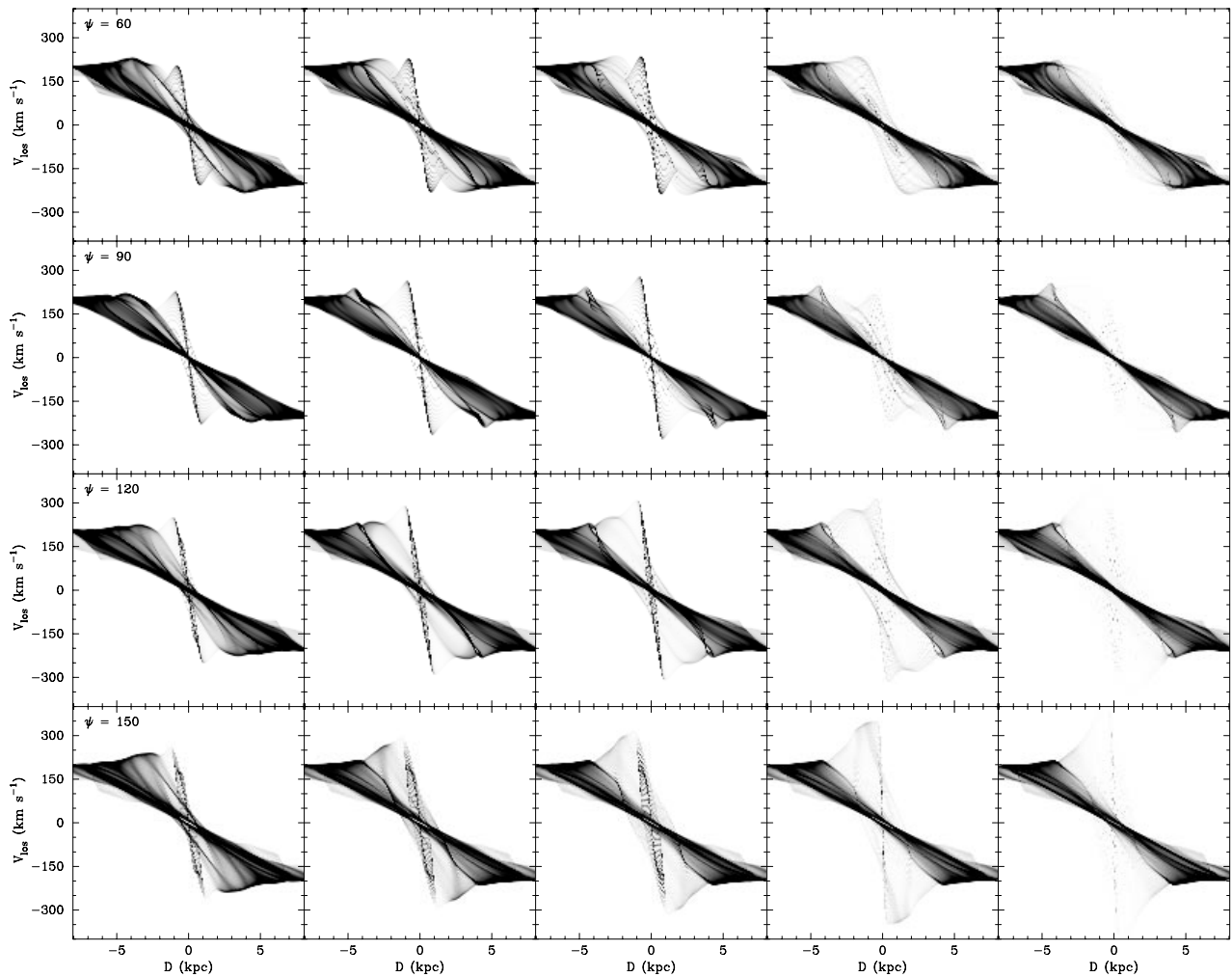
Fig. 6.—Continued

ratio is increased (see Fig. 6 of A92a), the inverted S-shaped signature of the nuclear spiral in the PVDs disappears for large bar axial ratios. The maximum radial velocity reached by the nuclear spiral signature varies little with the bar axial ratio (when present).

Figure 7 shows how the PVDs of the simulated disks change when the Lagrangian radius of the mass model is varied. A92b showed that the gas flow in a bar has shock loci offset toward the leading sides of the bar and of the form observed in early-type barred spiral galaxies only for a restricted range of Lagrangian radii, namely $r_L = (1.2 \pm 0.2)a$. All the observational estimates for early-type strongly barred spirals also give values within this range (see, e.g., A92b; Elmegreen 1996). We will thus concentrate on this range here. Model 028, the limiting case with $r_L = 5.0$, shows strong spiral arms starting at the ends of the bar and extending to large radii. The spiral arms are easily identified in the PVDs as long filamentary structures. This model has no nuclear spiral, and thus no corresponding inverted S-shaped feature in the PVDs. The opposite is true for models with larger Lagrangian radii or, equivalently, lower pattern speeds. Those models have extended x_2 families of periodic orbits and therefore nuclear spirals (see A92b). As the pattern speed of the bar is further decreased, the radial range occupied by the x_2 periodic orbits is increased and the nuclear spiral becomes more predomi-

nant. The outer bar region decreases accordingly (A92a). This effect is clearly seen in the PVDs of Figure 7. For increasing Lagrangian radii, they show an increase of the radial extent of the nuclear spiral signature and a decrease of the radial extent of the outer bar region signature. There is also an increase of the maximum radial velocity reached by the nuclear spiral, but the effect is rather small.

Figure 8 shows the behavior of the PVDs as the central concentration of the mass model is varied. For low central concentrations, the gas streamlines are oval-shaped and aligned with the bar, there are no shocks, and the bar region is only slightly gas depleted. The signature of the bar region in the PVDs is then very strong. As the central concentration is increased, the streamlines become more eccentric and the envelope of the signature of the bar region extends to higher velocities. Once the central concentration reaches $\rho_c \approx 2.2 \times 10^4$, an x_2-like flow appears in the center of the bar and a nuclear spiral and offset shocks are formed. These changes are also easily seen in the PVDs, which acquire an inverted S-shaped feature, while the density in the outer bar region drops. The region occupied by the x_2 orbits then increases with increasing central concentration (A92a), and so does the radial extent of the nuclear spiral signature in the PVDs. An increase in the central concentration of the mass model has effects similar to an increase of the Lagrangian radius (see Fig. 7). This is not surprising, since
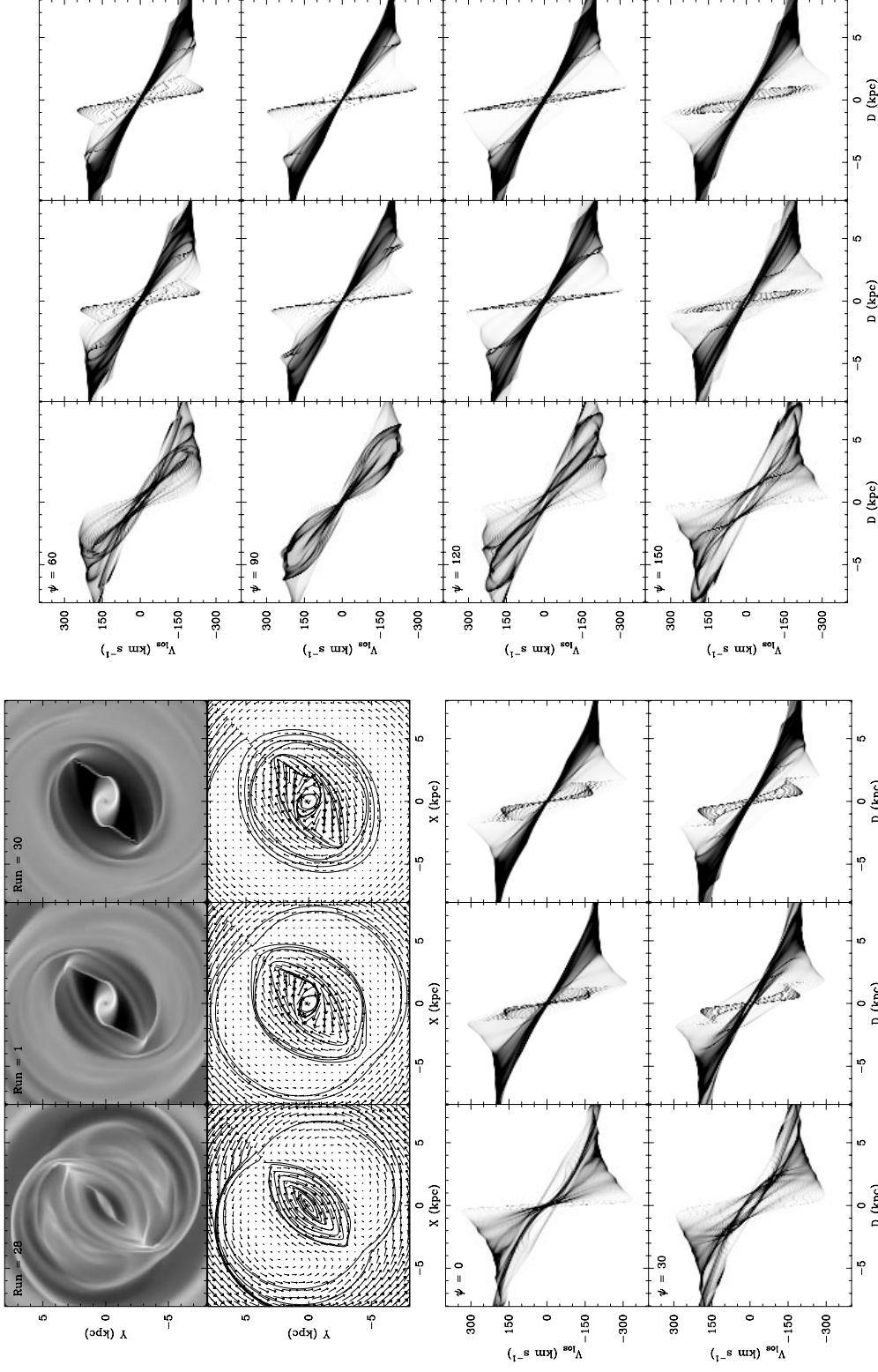
Fig. 7.—Same as Fig. 6, but for a sequence of models of increasing Lagrangian radius r_L. From left to right, the models are 028, 001, and 030, with $r_L = 5.0$, 6.0, and 7.0, respectively. The other parameters of the models are kept fixed at those of model 001 : $n = 1$, $a/b = 2.5$, $\rho_c = 2.4 \times 10^4$, and $Q_m = 4.5 \times 10^4$.
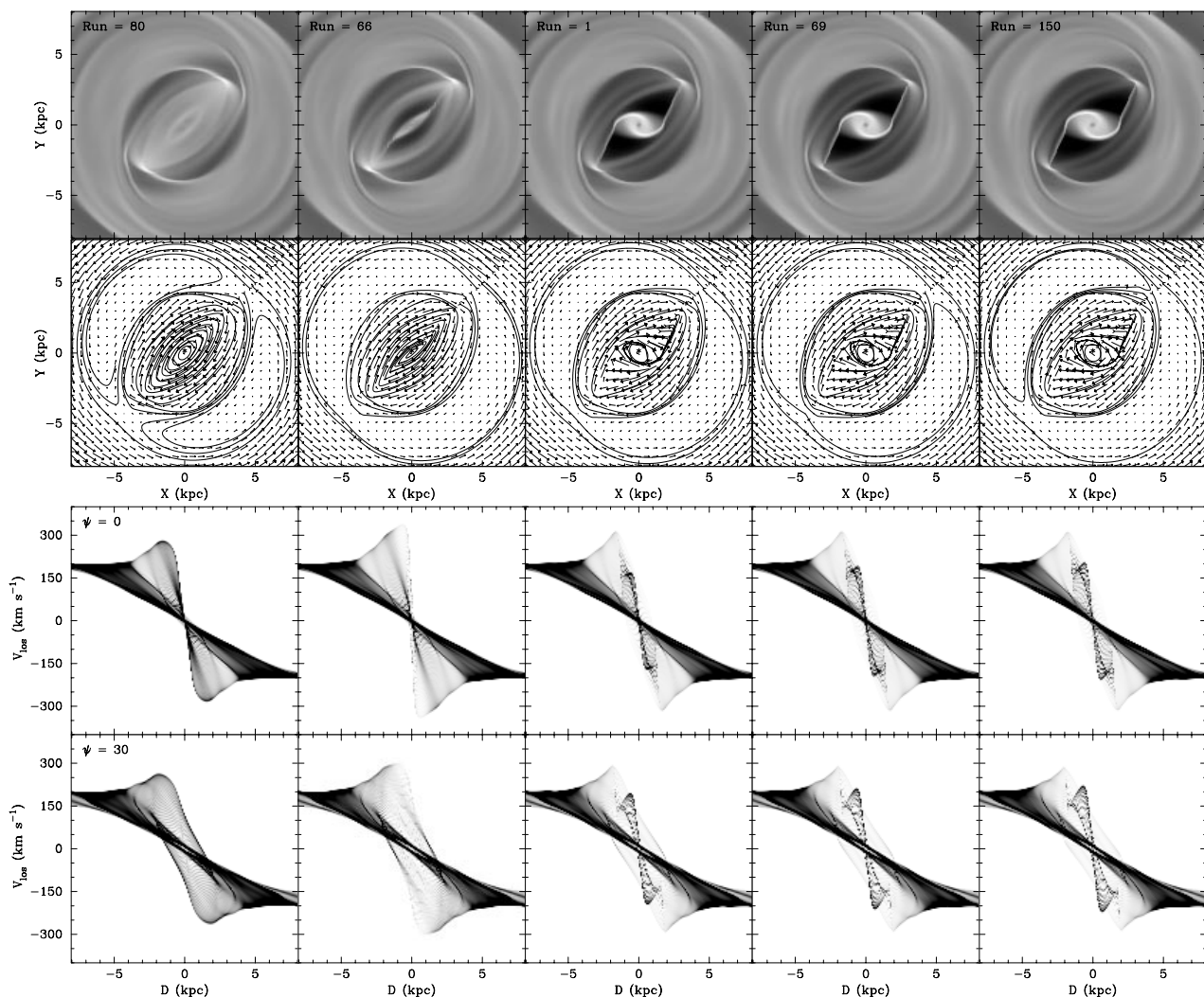
FIG. 8.—Same as Fig. 6, but for a sequence of models of increasing central density ρ_c. From left to right, the models are 080, 066, 001, 069, and 150, with $\rho_c = 0.4 \times 10^4$, 1.6×10^4, 2.4×10^4, 3.2×10^4, and 4.0×10^4, respectively. The other parameters of the models are kept fixed at those of model 001: $n = 1$, $a/b = 2.5$, $r_L = 6.0$, and $Q_m = 4.5 \times 10^4$.

both changes influence the location of the resonances in a similar way.

Figure 9 shows a sequence of simulations with varying bar quadrupole moment. For the lowest quadrupole moment, the bar is weak and the flow is close to circular, with only a weak nuclear spiral and curved shocks in the center. This does not cause substantial inflow, and the gas density in the barred region remains high. The velocity field shows that there is a transition from a x_1-like flow to a x_2-like flow in the central region, but the effect is not strong, since the eccentricity of the streamlines is small. All these effects reflect themselves in the PVDs. For somewhat higher bar quadrupole moments (model 058), the nuclear spiral is well developed and its signature is strong in the PVDs, with a gap present between it and the solid-body signature of the outer parts of the galaxy. As the bar quadrupole moment is increased further, the envelope of the signature of the outer bar region in the PVDs becomes more extreme, reaching larger radial velocities and extending closer to the center. For $Q_m \gtrsim 5.5 \times 10^4$, the nuclear spiral disappears. Those two effects are due to the fact that the eccentricity of the streamlines increases significantly with increasing bar quadrupole moment, while the region occupied by the x_2 orbits

decreases until it disappears completely (see A92a). Because the bar is so strong for high quadrupole moments, the flow is noncircular even in the outer parts of the simulations, and a "hole" is present in the center of the PVDs at intermediate viewing angles. Not surprisingly, the variations in the gas distribution and kinematics are similar when the bar quadrupole moment is increased and when the axial ratio of the bar is increased.

4. DUST EXTINCTION

It is interesting to note that the PVDs discussed so far have a certain degree of symmetry with respect to the viewing angles $0°$ or $90°$. This means that although it is relatively easy to determine whether a line of sight is close to the major or the minor axis of a bar ($|\psi|$), it is considerably more difficult to determine in which half of the PVD (positive or negative projected distances from the center) the near side of the bar is located ($\pm \psi$).

This situation can be contrasted to that in the Galaxy, where most studies have no difficulty identifying the quadrant in which the near side of the Galactic bar is located. Studies using infrared photometry (e.g., Dwek et al. 1995; Binney, Gerhard, & Spergel 1997), star counts (e.g., Wein-
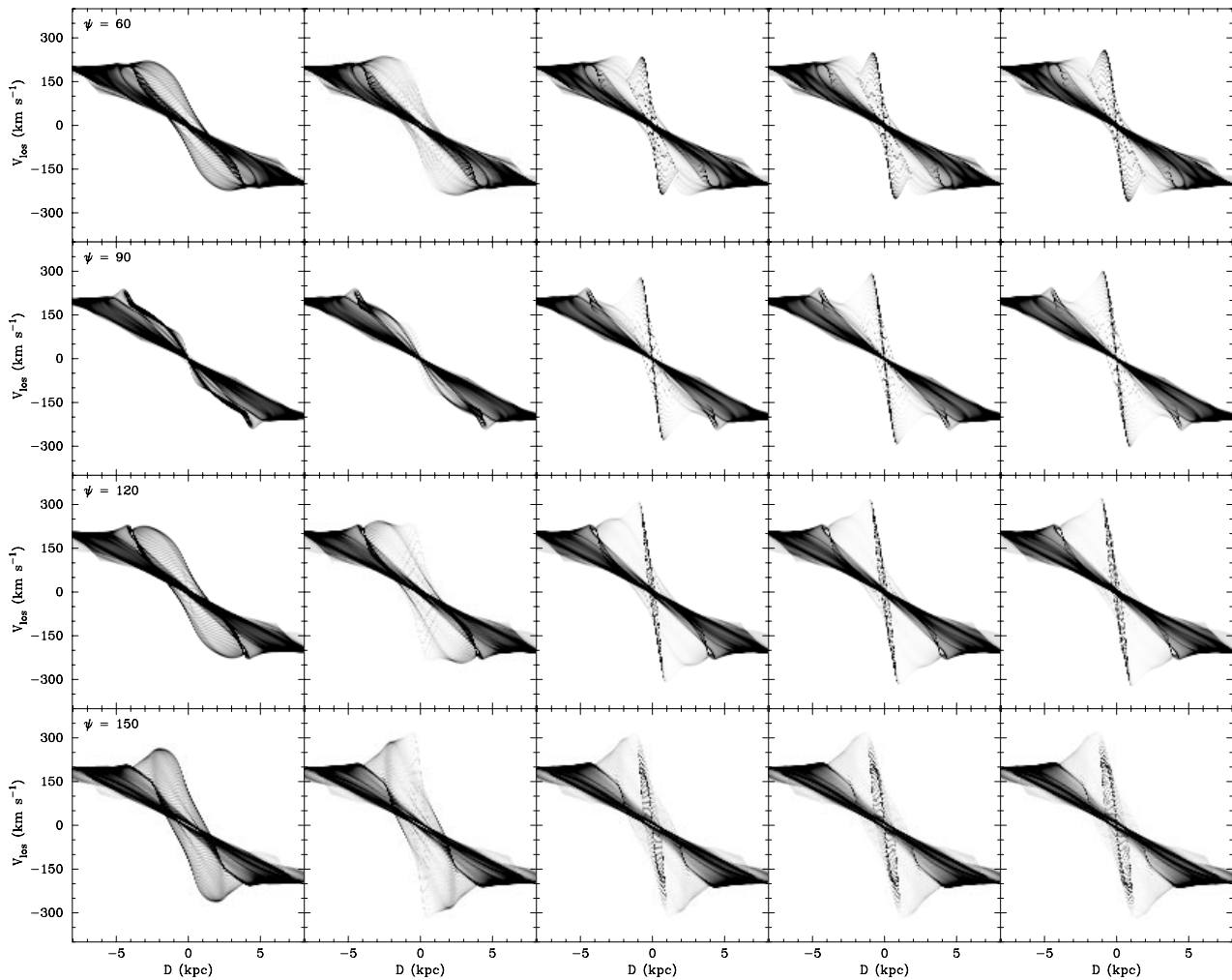
FIG. 8.—*Continued*

berg 1992; Stanek et al. 1997), gaseous or stellar kinematics (e.g., Binney et al. 1991; Wada et al. 1994; Zhao, Spergel, & Rich 1994; see also Beaulieu 1996, and microlensing events (e.g., Paczynski et al. 1994) all indicate a bar making an angle of 15° to 45° with respect to the line of sight to the Galactic center (positive values indicating that the near side of the bar is at positive Galactic longitude). In the case of the Galaxy, at least two effects help the observer determine the exact orientation of the bar. First, projection effects (in both longitude and latitude) mean that two lines of sight on each side of the Galactic center reach correspondingly different parts of the bar (e.g., Binney et al. 1991). Second, the large difference between the distances to each side of the bar means that point sources in the far side of the bar appear significantly fainter than the corresponding sources in the near side (e.g., Stanek et al. 1997). In addition, the far side of the bar will appear thinner than the near side (Dwek et al. 1995). For a galaxy at infinity, all lines of sight are parallel, and no projection or distance effects are present. However, extinction within an edge-on disk can play a role similar to that of distance in the Galaxy, and can help constrain the orientation of a bar. Because the velocity spread in the inner parts of the PVDs is so large, it is unlikely that self-absorption by any line would be significant. Given the prominence of the dust lanes in many edge-on spiral galaxies, extinction by dust is likely to be the dominant factor

affecting the PVDs. If dust is present in any significant amount, the spectroscopic signature of the far side of the bar in a PVD should be fainter than that of the nearer side.

Figure 10 shows the surface density and PVDs of model 001 when considering a dust distribution proportional to the gas surface density. Because our simulations are not self-consistent, only the relative values of the density are important, and the exact value of the dust absorption coefficient per unit mass, κ, we use is meaningless. Since our goal in this section is merely to illustrate the effects of dust on the simulated PVDs, and not to reproduce quantitatively the situation in real galaxies, we have simply increased the value of κ (in which the dust-to-gas ratio is also folded) until the PVDs were significantly affected. In Figure 10, we have also decreased the surface densities in the surface-density plot to reflect the effective contribution of each point to the projected density for a viewing angle $\psi = 45°$. Unlike Figure 1, the PVDs are now far from symmetric with respect to viewing angles of 0° or 90°. In addition, PVDs at intermediate viewing angles are no longer antisymmetric with respect to the center. This is mainly because the nuclear spiral obscures most of the material behind it, breaking the symmetry of the parallelogram-shaped signature of the x_1-like flow in the outer bar region. For viewing angles of $0° \lesssim \psi \lesssim 90°$, the nuclear spiral obscures mostly material moving away from the observer in the outer bar
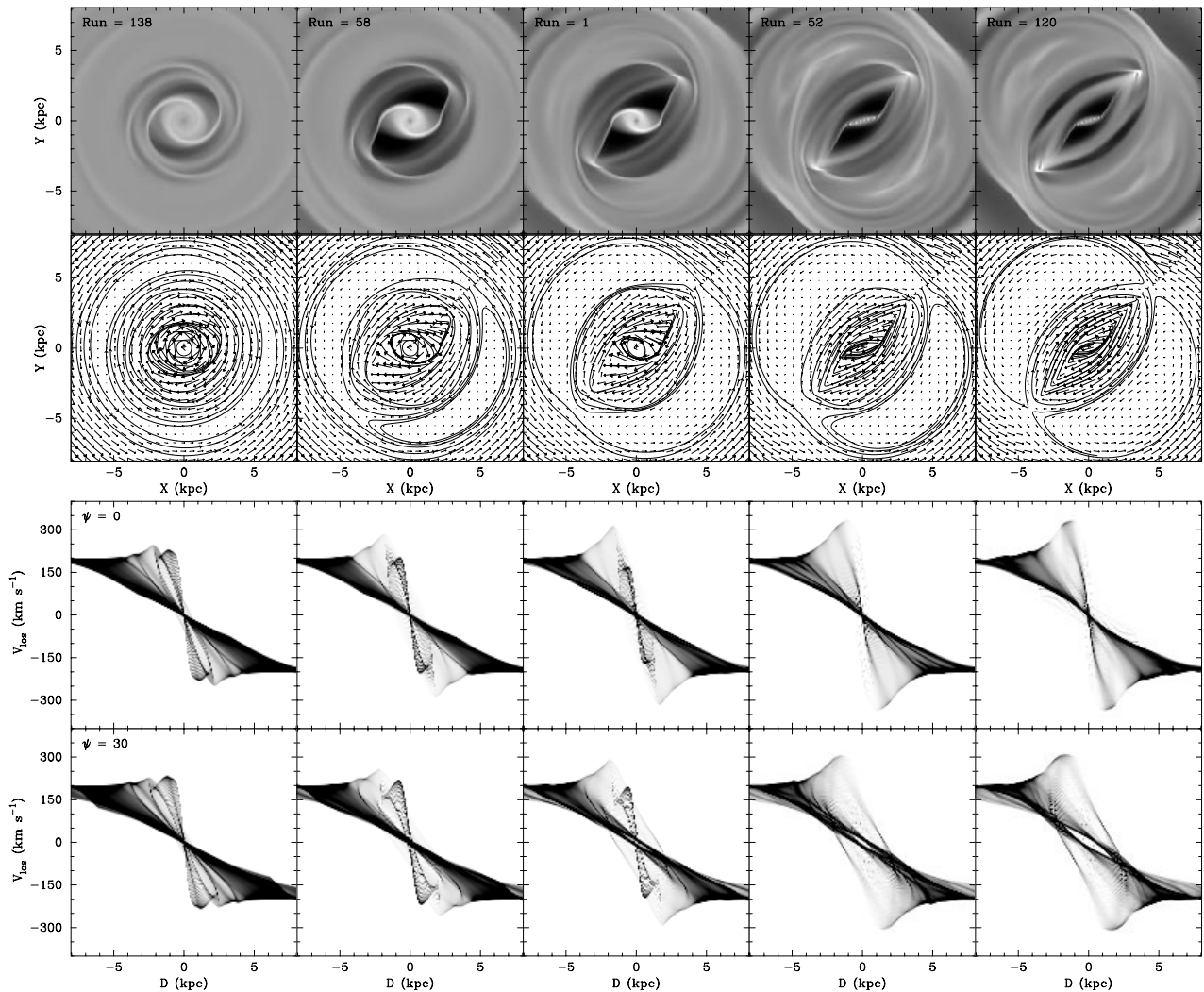
FIG. 9.—Same as Fig. 6, but for a sequence of models of increasing bar quadrupole moment Q_m. From left to right, the models are 138, 058, 001, 052, and 120, with $Q_m = 0.5 \times 10^4$, 2.5×10^4, 4.5×10^4, 6.0×10^4, and 8.0×10^4 respectively. The other parameters of the models are kept fixed at those of model 001: $n = 1$, $a/b = 2.5$, $r_L = 6.0$, and $\rho_c = 2.4 \times 10^4$.

region, and only a small amount of material moving toward the observer in the same region. Thus, the signature of the x_1-like flow in the PVDs is weakened for positive radial velocities, leading to a much fainter signature of the outer bar region in the upper halves of the PVDs than in the lower halves. The opposite is true for viewing angles of $90° \lesssim \psi \lesssim 180°$, where the signature of the outer bar region is much fainter in the lower halves. This effect is strongest and least extended for viewing angles of $\psi \approx 110°–135°$, since the line of sight is then roughly parallel to the major axis of the nuclear spiral (which is slightly offset from that of the x_2 periodic orbits). Some effects on the signature of the nuclear spiral itself and on the signature of the outer parts of the simulation are present, but they are less pronounced.

In addition to the diagnostics suggested in the previous sections to identify a bar in an edge-on spiral galaxy and determine whether it is seen end-on or side-on, the introduction of dust in the simulations has allowed us to develop criteria to determine in which half of the galaxy the near side of the bar is located. Of course, the distribution of dust in real galaxies will inevitably be more complex than the highly idealized distribution adopted here. Nevertheless, the features due to dust in the PVDs of Figure 10 can probably

still be used as a guide to interpret asymmetries present in real data.

5. DISCUSSION

5.1. Bar Diagnostics

Unlike periodic orbits studies (KM95; Paper I), in which one must adopt a way of populating the orbits, hydrodynamical simulations provide both the velocity and density of the gas. In particular, if some periodic orbit families intersect, it is not necessary to make a choice between them, because the simulations will reveal which family the gas follows in each region (and to what extent). Nevertheless, as we will discuss later in this section, the comparison with observations can still present some problems, since observations involve the strength of a given emission line rather than the gas density.

Notwithstanding the problem of populating the orbits, there is generally a good agreement between the PVDs obtained from periodic orbit calculations in Paper I and those obtained here from hydrodynamical simulations. This is because there are several similarities between the periodic orbits structure of the models and the gas flow (A92b). In
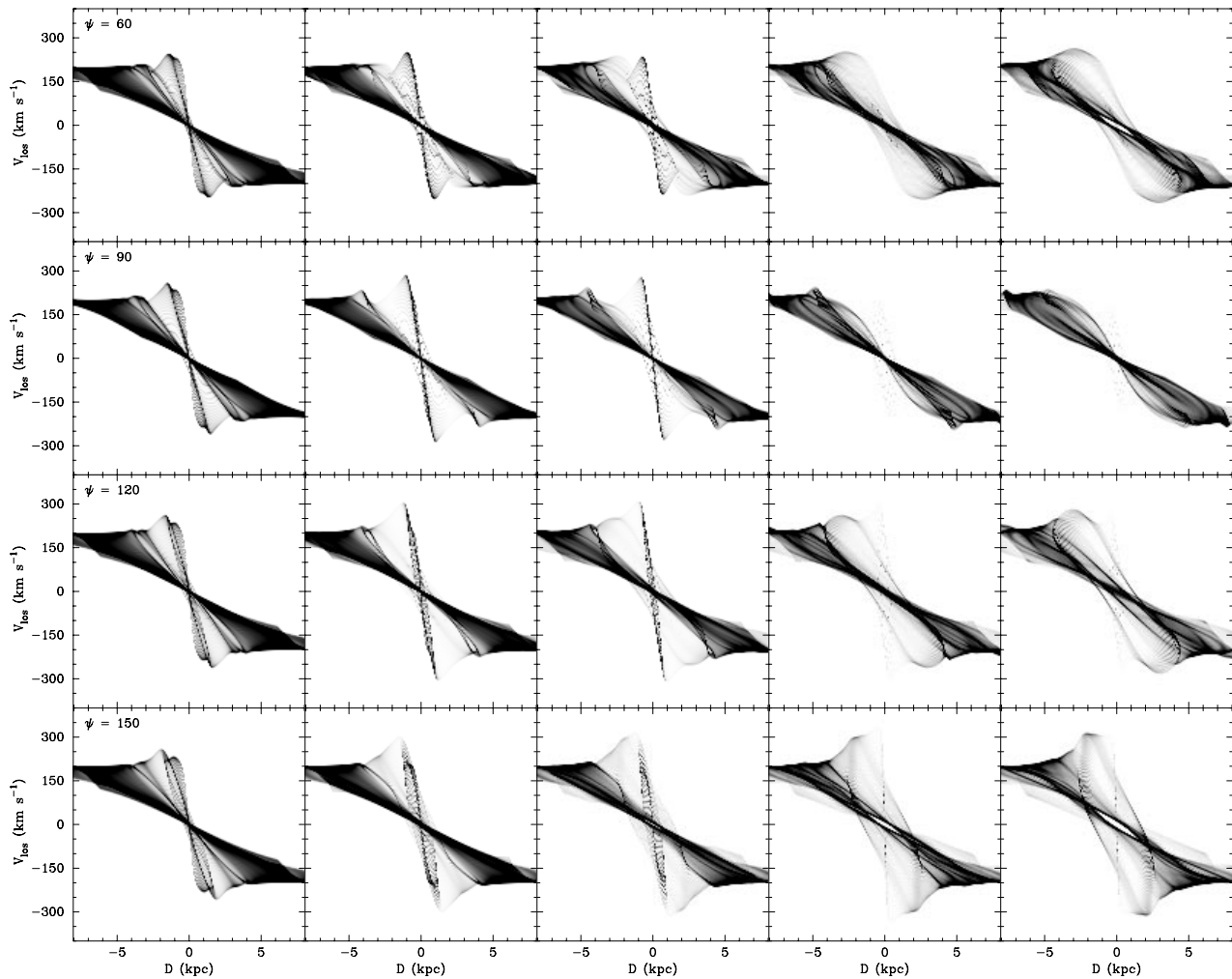
Fig. 9.—*Continued*

both cases we have a central PVD component, which we identify in Paper I with the x_2 orbits and in this paper with the nuclear spiral. Farther out, we have the domain of the x_1 orbits, which covers the outer (or entire) bar regions of the simulations. In Paper I, by studying in detail the signatures of various periodic orbit families in the PVDs, we gained useful insight into the projected structure and kinematics of the gas from first principles. This allowed us to gain a deeper understanding of the PVDs produced in the hydrodynamical simulations.

The main feature of the PVDs is the gap (fainter region), present at all viewing angles, between the signature of the nuclear spiral and that of the outer parts of the simulations. Such a structure would not be possible in an axisymmetric galaxy, and it unmistakably reveals the presence of a bar or oval in an edge-on disk. This gap occurs because of the large-scale shocks that are present in bars, driving an inflow of gas toward the center and depleting the outer bar regions.

The gaps present in the PVDs produced with periodic orbits (see KM95; Paper I) are different in nature from the ones observed here, being mainly due to the absence of populated orbits in certain regions of the models, particularly near corotation. As a result, in these studies, the low-

density region extends well beyond corotation, although its exact extent depends on which orbits are neglected (e.g., as self-intersecting) and how the other orbits are populated. For example, in Figure 1 of KM95, the gap extends to almost twice the corotation radius.

We recall that three-dimensional N-body simulations of rotating disks produce bars which, when viewed edge-on, appear boxy-shaped if seen end-on and peanut-shaped if seen side-on (see, e.g., Combes & Sanders 1981; Combes et al. 1990; Raha et al. 1991). Taking the maximum height of the peanut-shaped bars to occur at half the corotation radius (Combes et al. 1990), we find that, in the KM95 case, the ratio of the radial extent of the gap in the PVDs to the radius at which the maximum height of the peanut-shaped bulges occurs should be approximately 4 (or slightly less because of projection effects; associating the bulges with edge-on bars). On the other hand, in the hydrodynamical simulations presented here, the low-density region of the PVDs reflects the low-density region in the outer parts of the bar, and should thus be within corotation. When a bar is seen side-on, the ratio of the extent of the gap to the radius of the maximum height of the peanut-shaped bulge should thus be approximately 2 (or slightly less). KM95 report that this ratio is about 2 for the two galaxies they
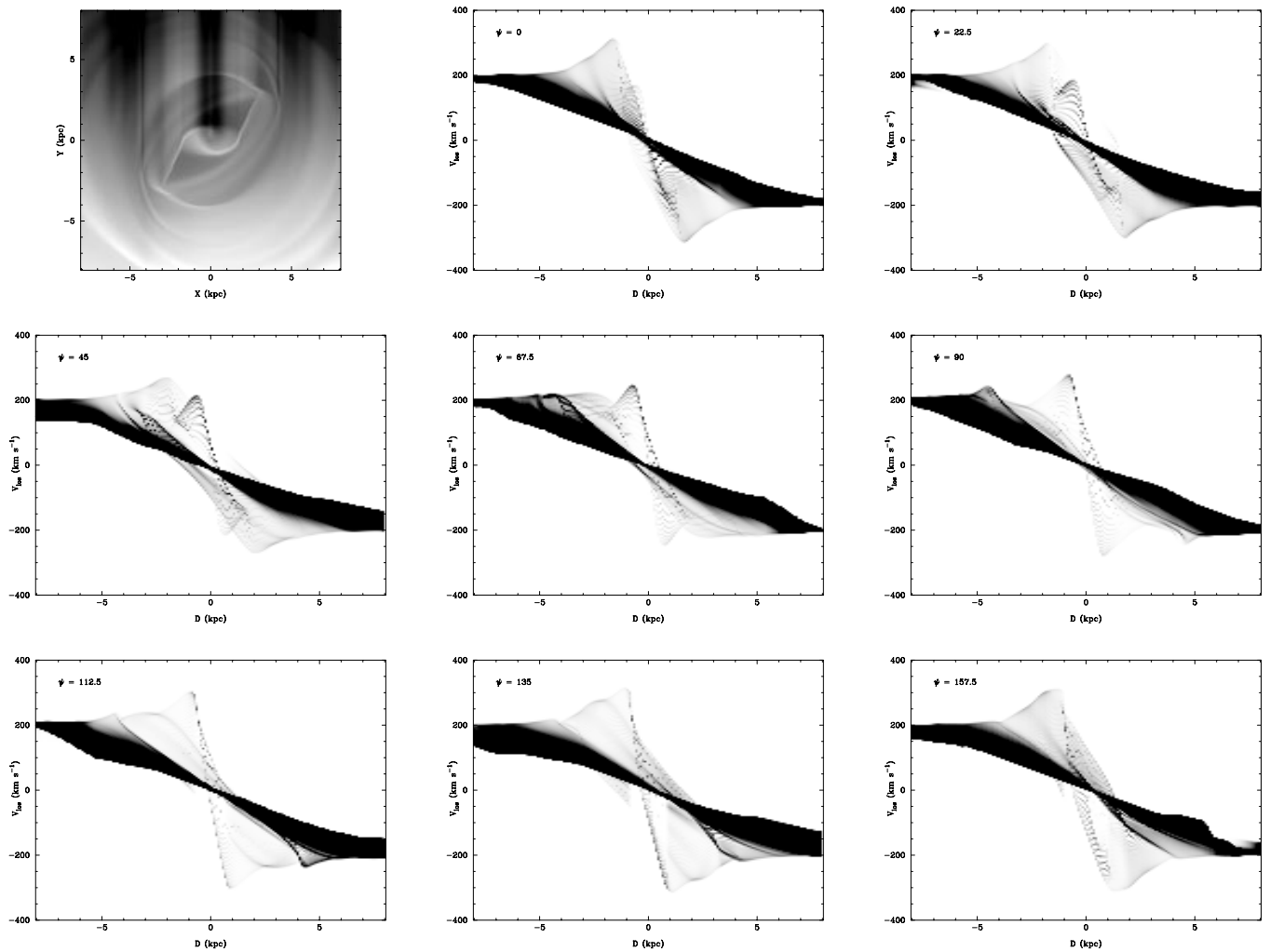
FIG. 10.—Same as Fig. 1, but considering a dust distribution proportional to the gas surface density. The absorption coefficient per unit mass is $\kappa = 0.1$. The surface densities in the top left plot have been decreased to reflect the effective contribution of each point to the integrated density along the line of sight for a viewing angle of $\psi = 45°$. New features in the PVD for $\psi = 45°$ can thus be directly related to new features in the surface density plot just above it.

studied, in agreement with the prediction of our hydrodynamical simulations. The same can be said for the galaxies studied by Bureau & Freeman (1997) and BF99. These results can only be reconciled with the periodic orbits approach if the maximum height of the peanut-shaped bulges occurs near corotation (rather than half-way).

As we pointed out in § 3.1, the shapes of the features present in the PVDs vary with the viewing angle, so they can in principle be used to constrain that quantity in an observed galaxy. The envelope of the signature of the outer bar region in the PVDs reaches very high radial velocities (compared to those in the outer parts of the simulations) for viewing angles close to the bar, and relatively low velocities for viewing angles perpendicular to it. However, the envelope is so faint in most cases (see § 3.3) that it is unlikely to be of much use with real data. The signature of the nuclear spiral has an inverted S-shape for some viewing angles and is almost solid-body for others. Unfortunately, that feature is rather thick and does not show much fine structure, however, so it may be difficult to use in conjunction with observations. The best viewing angle diagnostic is probably provided by the ratio of the maximum radial velocity reached by the nuclear spiral component to the velocity in the outer parts of the galaxy. This ratio should be greater than unity for viewing angles roughly perpendicular to the bar and smaller than unity for viewing angles parallel to it. Analyzing their sample, BF99 find that the above prediction is in good agreement with their results, provided that they make the reasonable assumption that bars are peanut-shaped when seen close to side-on and boxy-shaped when seen close to end-on (see, e.g., Combes & Sanders 1981; Combes et al. 1990). Other properties of the PVDs, such as the maximum radial velocity reached or the faintness of the signature of the outer (or entire) bar regions, can also help to constrain the mass distribution and bar properties of an observed galaxy (see § 3.3). In practice, however, the analysis and modeling of spectroscopic data should not be a trivial task.

If a barred system has no nuclear spiral (or, equivalently, does not have an extended x_2 family of periodic orbits), there will be no nuclear spiral signature in the PVDs and no gap, or double-peaked structure. In addition, the surface density in the bar region can be extremely low. An example of such a model was discussed in § 3.2 (model 086). In such

cases, the only component likely to be detected observationally is the solid-body signature of the outer parts of the galaxy, and the kinematical detection of the bar will not be straightforward. The first step would be to rule out such a slowly rising rotation curve (the rotation curve being defined as the upper limit of the envelope of the observed PVD), for example by calculating the shape of the rotation curve expected from surface photometry. Unfortunately, this would only show that the type of gas observed (ionized, neutral, or molecular) is not present in large quantities in the central region of the galaxy, but it would not provide any information on the cause of this depletion. It is thus probably necessary to use stellar kinematics to identify a bar in such systems. Because a large percentage of the stars in the central regions of barred disks are expected to be trapped around the x_1 orbits, there should be a clear bar signature in the PVDs. We will explore possible diagnostics based on the stellar kinematics (and corresponding PVDs) in Paper III.

Cases with no nuclear spiral component should be a minority, however, at least among strongly barred early-type spiral galaxies, since observational evidence argues that these systems possess ILRs (see, e.g., Athanassoula 1991; A92b). In particular, the fact that the dust lanes in most early-type strongly barred galaxies are offset along the leading sides of the bar, rather than centered and close to its major axis, is a strong argument for the existence of ILRs (A92b). In addition, out of 17 galaxies with a boxy/peanut-shaped bulge in the sample of BF99, only four have no nuclear component in their PVD. The absence of a nuclear component in these four galaxies could be due to the lack of ILRs, but also to the lack of emitting gas around the ILR region. At any rate, at least 13 out of 17 galaxies, i.e., an overwhelming majority, have ILRs. Nevertheless, the existence of ILRs deserves further study, particularly for later-type spirals. This could be done, for example, by high-resolution kinematical studies, to show the change of direction of the orbits or streamline ellipticities in the central parts of galaxies (e.g., Teuben et al. 1986), or by calculating the families of periodic orbits in galaxy potentials derived from observations, to show the existence or nonexistence of the x_2 (and x_3) family.

5.2. NGC 5746–like PVDs

Although our simulations cover a fair fraction of the available parameter space (see Table 1 in A92a), we have never come across a PVD showing a clear "figure eight," as suggested by KM95. In other words, the upper envelope of the low-density region of the simulated PVDs is never as pronounced as it is in NGC 5746 or, to a lesser extent, in NGC 5965 and NGC 6722 (see KM95; Bureau & Freeman 1997; BF99).

Based on periodic orbits calculations, we expect this region of the PVDs to originate from material near the ends of the bar on its *minor* axis (see, e.g., Fig. 2b in Paper I). Some models, particularly $n = 0$ models, indeed have secondary density enhancements near the edge of the bar, just outside the offset shocks that we have already discussed (see Fig. 3 in A92b). These enhancements are due to the small distance between the outer ILR and the tip of the x_1 family characteristic curve in the characteristic diagram (A92b). This leads to orbit crowding, particularly near the bar minor axis. In these models, the upper envelope of the gap in the PVDs is stronger than in most other models.

Figure 11 shows two density distributions for model 088 and the corresponding PVDs for a viewing angle $\psi = 45°$. On the left (Figs. 11a and 11b), the entire density distribution and PVD are displayed. On the right (Figs. 11c and 11d), most of the PVD was masked out, leaving only the region of interest in objects such as NGC 5746. The corresponding density distribution was obtained using a simple inversion scheme. The strong upper envelope of the low-density region of the PVD is clearly due to the secondary density enhancement on the leading side of the bar. A similar effect is observed in many $n = 0$ models with low bar axial ratio a/b, small Lagrangian radius r_L, and/or low central concentration ρ_c (e.g., models 013–016, 040–043, 061–063, 087–088, and 108–110). Although the intensities obtained in these simulations are much lower than the strong envelopes observed in objects such as NGC 5746, we must remember that it is the density that is plotted here, and the gaseous emission in the secondary density enhancements could be somehow enhanced, e.g., through shocks. Features similar to those density enhancements are observed in real barred galaxies, where "plumes" are sometime seen on the leading sides of bars (in NGC 1365, for example). We suggest here that these plumes may be responsible for the strong upper envelope of the gap observed in the PVD of some galaxies.

We must stress, however, that a strong envelope is unusual; it is absent from the PVDs of most galaxies. In the sample of BF99, only two galaxies out of 17 present clear indications of such a feature. This seems to be in agreement with the explanation presented above, since strong plumes are not often observed.

5.3. Limitations of the Models

When using the bar diagnostics developed in this paper to interpret observational data, one must take into account the fact that the PVDs were calculated using the gas *density* in the simulations and not the strength of a given gaseous emission line, which is what one usually observes. The physical conditions in the gas vary across the simulated disks, and will lead to different excitation mechanisms dominating in different parts of the disks. Regions of high density and low shear are likely to have higher star formation rates and thus more photoionized gas than elsewhere. Conversely, the gas in or near shocks, such as the nuclear spiral, will be mainly shock-excited (see Binette, Dopita, & Tuohy 1985; Dopita & Sutherland 1996), with possible star formation depending on the shear. Because different excitation mechanisms lead to different emission-line ratios, the relative amplitudes of the various components of a PVD (e.g., the intensity of the signature of the outer parts of the disk versus that of the nuclear spiral) will depend on the emission line used in the observations. For example, Bureau & Freeman (1997) and BF99 found that, for many objects, the signature of the nuclear spiral was very strong in the [N II] $\lambda6548, 6584$ lines but was almost absent in Hα, probably indicating that it is shock-excited (the other components of the PVDs showed [N II] $\lambda6584$/Hα ratios typical of H II regions). The PVDs were not corrected for stellar absorption, however, so these results should be interpreted with caution. Nevertheless, the PVDs produced here should only be used as a guide when interpreting kinematical data, and one should have a basic understanding of the mechanisms involved in the production of a given line before using PVDs for comparison purposes. We stress that the mor-
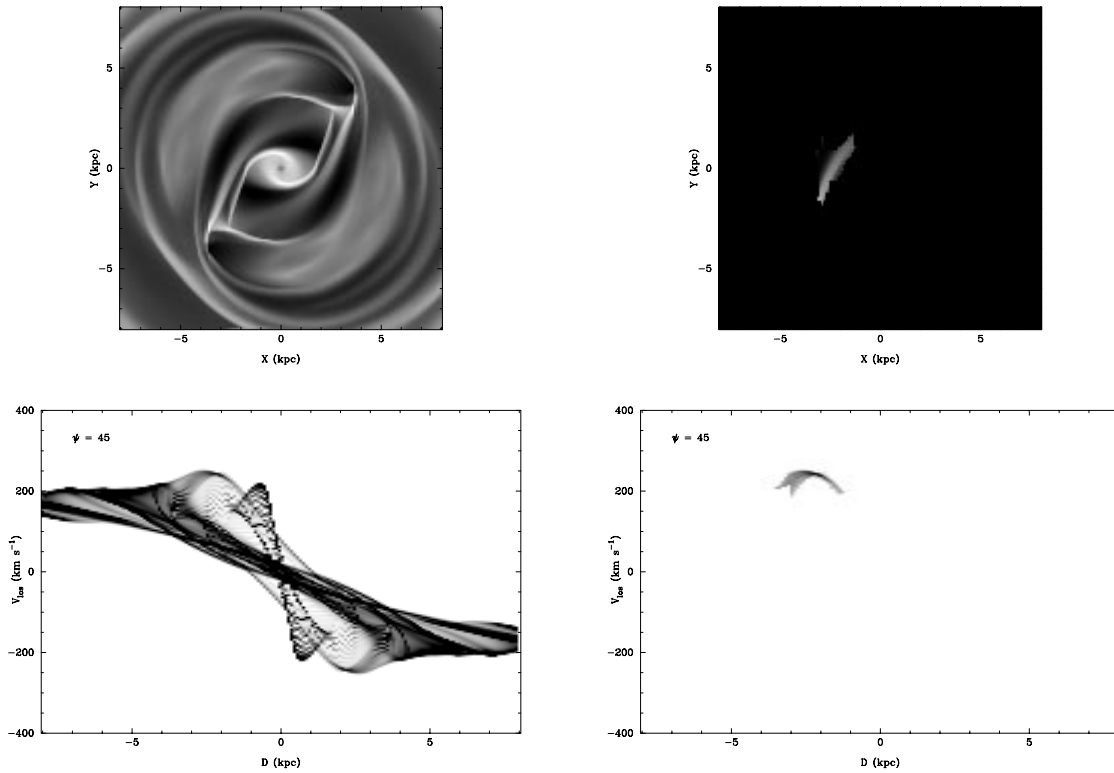
FIG. 11.—Gas distributions and position-velocity diagrams of model 088, with $n = 0$, $a/b = 3.0$, $r_L = 5.5$, $\rho_c = 2.4 \times 10^4$, and $Q_m = 4.5 \times 10^4$. (a) The face-on logarithmic gas surface density of the simulation. We use logarithmic values (in the density plots alone) because the dynamic range of the gas surface density is high. Dark shading denotes low-density regions. The bar is at 45° to the horizontal, has a semimajor axis length of 5 kpc, and is rotating clockwise. (b) The position-velocity diagram (projected density of material as a function of line-of-sight velocity and projected position along the major axis) of the gas when the simulation is viewed edge-on. For this plot, dark shading denotes high-density regions. The angle between the line of sight and the bar is $\psi = 45°$, a viewing angle of $\psi = 0°$ indicating that the bar is seen end-on (line of sight parallel to the bar) and a viewing angle of $\psi = 90°$ indicating that the bar is seen side-on (line of sight perpendicular to the bar). The viewing angle increases counterclockwise in the surface density plots. (c)–(d) Same as (a)–(b), except that most of the simulation has been masked out. Only the upper envelope of the low-density region of the PVD has been kept, as well as the corresponding region of the density distribution, obtained using a simple inversion scheme.

phology of the PVDs (the multiple components) is a more significant bar diagnostic than the distribution of intensity (the relative amplitude of the components).

Conversely, under certain assumptions about the physical conditions in the gas, it is possible to use the observed emission line ratios (e.g., Hα/Hβ) to measure the extinction due to dust in data. This could prove useful in interpreting asymmetries in observed PVDs (see § 4 for a more complete discussion of likely dust effects).

Contrary to the "building-blocks" approach of Paper I, which used combinations of periodic orbit families to model the structure and kinematics of barred galaxies, the hydrodynamical simulations presented here inherently take into account the collisional nature of gas, so the kinematics of the gaseous component is more accurately modeled. Approximations to the gas properties are nevertheless necessary, and we recall that the gas was treated as ideal, isothermal, infinitely thin, and non–self-gravitating. How much do our results depend on these assumptions, or, in other words, how model-dependent are they?

The interstellar medium is a complicated multiphase mixture, which can only be described schematically, particularly in nonlocal studies covering an object the size of a galaxy. Two different approaches have been developed so far. In the first, the gas is treated as ballistic particles which, when they collide, lose energy according to prespecified

recipes (e.g., Miller, Prendergast, & Quirk 1970; Schwarz 1981, 1984; Combes & Gerin 1985). Unfortunately, the results of these simulations can depend on the adopted collision law (Guivarch & Athanassoula 1999), at least as far as the shocks in the barred region are concerned. In the second approach, a hydrodynamical treatment is used, solving the Euler equations with the help of a grid (e.g., van Albada & Roberts 1981; van Albada, van Leer, & Roberts 1982; Mulder 1986; Piner, Stone, & Teuben 1995), smoothed particle hydrodynamics (SPH; Lucy 1977; Gingold & Monaghan 1977; Hernquist & Katz 1989; etc.), or beams (Sanders & Prendergast 1974). A number of these studies assume an isothermal equation of state, following the model of Cowie (1980), who calculated the equation of state for an ensemble of clouds and found that it could be described as isothermal, provided that the clouds have an equilibrium mass spectrum.

Comparing the results of all these schemes is beyond the scope of this paper. In all approaches, the more reliable codes produce shocks in the bar region that are more or less offset from the bar major axis toward its leading sides. These shocks result in an inflow of gas and a substantial lowering of the density in the outer bar region. Although the precise location, shape, and persistence of the shocks differ, these are relatively small effects compared to the fact that we weight by density rather than by the strength of an

emission line. The main reason for adopting the present hydrodynamical code is that it has given very good results in many previous studies (see A92b).

Because dissipation ensures that the gas layer in spiral galaxies remains thin, the two-dimensional nature of the simulations should not limit the applicability of the results to the interpretation of real data. Furthermore, vertical motions have no direct consequence on the PVDs produced, since the movement is perpendicular to the line of sight. It is somewhat more difficult to gauge the consequences of the fact that we have ignored the gas self-gravity. Because our mass model represents best (barred) early-type spirals (see A92a), in which the fraction of the total mass in gas is typically less than 10%, the contribution of the gas to the potential and large-scale forces is negligible. Indeed, Lindblad, Lindblad, & Athanassoula (1996) found that including self-gravity in their model of NGC 1365 made very little difference to the global picture. It may well be, however, that near high-density structures such as the nuclear spiral, the self-gravity of the gas is important.

6. SUMMARY AND CONCLUSIONS

Our main aim in this paper, the second in a series, was to develop diagnostics to identify bars in edge-on spiral galaxies using the particular kinematics of the gaseous component of barred disks. To achieve this goal, we ran two-dimensional hydrodynamical simulations of the gas flow in the potential of a barred spiral galaxy mass model. We constructed position-velocity diagrams (PVDs) from those simulations, using an edge-on projection and various viewing angles with respect to the major axis of the bar. The presence of shocks and inflows in the simulations allowed us to develop better bar diagnostics than those presented in our first paper (Bureau & Athanassoula 1999), which were based on periodic orbits calculations.

We analyzed in detail two simulations that are prototypes of simulations for models with and without inner Lindblad resonances (which we associate with the existence of x_2 periodic orbits). We showed that for models allowing x_2 orbits, the nuclear spiral created in the center of the simulations produces a strong inverted S-shaped signature in the PVDs. This signature reaches high radial velocities (compared to those in the outer parts of the simulations) when the bar is seen side-on, and relatively low velocities when the bar is seen end-on. The flow in the outer bar region (the entire bar region if no nuclear spiral is present) produces a parallelogram-shaped signature in the PVDs, being associated with the x_1 periodic orbits. Because the flow is mostly along the bar in that region, the highest velocities are now reached for viewing angles close to the bar major axis. In the outer parts of the simulations, the flow is almost circular and produces a strong, almost solid-body signature in the PVDs for all viewing angles.

Shocks within the bar are present in most simulations and lead to a depletion of the gas in the region of the bar occupied by an x_1-like flow. Thus, if a nuclear spiral is present, a bar can easily be identified in an edge-on spiral galaxy, since there will be a gap in the PVD between the signature of the nuclear spiral and that of the outer parts of the galaxy. If there is no nuclear spiral, it may still be possible to detect a bar, but only with the help of photometry and/or stellar kinematics. The envelope of the signature of the nuclear spiral, and to a lesser extent that of the outer bar region, is most useful to determine the orientation of a bar with respect to the line of sight. It is nevertheless difficult to discriminate between two viewing angles on either side of the bar. We showed that adding dust to the simulations helps break this degeneracy.

We also produced PVDs for a range of simulations covering most of the fraction of parameter space likely to be occupied by real galaxies. These simulations can be used to constrain the mass distribution and bar properties of an observed system. In particular, the presence or absence of the signature of a nuclear spiral in a PVD places strong constraints on the values the parameters of our mass model may take. The nuclear spiral can be absent for high bar axial ratios and/or bar quadrupole moments, and for low Lagrangian radii and/or central concentrations.

REFERENCES

Athanassoula, E. 1991, in Dynamics of Disk Galaxies, ed. B. Sundelius (Göteborg: Chalmers Univ. Technology), 149
———. 1992a, MNRAS, 259, 328 (A92a)
———. 1992b, MNRAS, 259, 345 (A92b)
Athanassoula, E., Bienayme, O., Martinet, L., & Pfenniger, D. 1983, A&A, 127, 349
Athanassoula, E., & Bureau, M. 1999, in preparation (Paper III)
Beaulieu, S. F. 1996, Ph.D. thesis, The Australian National Univ.
Binette, L., Dopita, M. A., & Tuohy, I. R. 1985, ApJ, 297, 476
Binney, J., Gerhard, O., & Spergel, D. 1997, MNRAS, 288, 365
Binney, J., Gerhard, O. E., Stark, A. A., Bally, J., & Uchida, K. I. 1991, MNRAS, 252, 210
Bureau, M., & Athanassoula, E. 1999, ApJ, 521, this issue (Paper I)
Bureau, M., & Freeman, K. C. 1997, Proc. Astron. Soc. Australia, 14, 146
———. 1999, AJ, in press (BF99)
Combes, F., Debbasch, F., Friedli, D., & Sanders, R. H. 1990, A&A, 233, 82
Combes, F., & Gerin, F. 1985, A&A, 150, 327
Combes, F., & Sanders, R. H. 1981, A&A, 96, 164
Cowie, L. L. 1980, ApJ, 236, 868
de Carvalho, R. R., & da Costa, L. N. 1987, A&A, 171, 66
Dopita, M. A., & Sutherland, R. S. 1996, ApJS, 102, 161
Dwek, E., et al. 1995, ApJ, 445, 716
Elmegreen, B. 1996, in ASP Conf. Ser. 91, Barred Galaxies, ed. R. Buta, D. A. Crocker, & B. G. Elmegreen (San Francisco: ASP), 197

Ferrers, N. M. 1877, Q. J. Pure Appl. Math., 14, 1
Gingold, R. A., & Monaghan, J. J. 1977, MNRAS, 181, 375
Guivarch, B., & Athanassoula, E. 1999, in preparation
Hamabe, M., & Wakamatsu, K. 1989, ApJ, 339, 783
Hernquist, L., & Katz, N. 1988, ApJ, 349, 562
Kuijken, K., & Merrifield, M. R. 1995, ApJ, 443, L13 (KM95)
Kuzmin, G. 1956, AZh, 33, 27
Lindblad, P. A. B., Lindblad, P. O., & Athanassoula, E. 1996, A&A, 313, 65
Lucy, L. B. 1977, AJ, 82, 1013
Merrifield, M. R. 1996, in ASP Conf. Ser. 91, Barred Galaxies, ed. R. Buta, D. A. Crocker, & B. G. Elmegreen (San Francisco: ASP), 179
Miller, R. H., Prendergast, K. H., & Quirk, W. J. 1970, ApJ, 161, 903
Mulder, W. A. 1986, A&A, 156, 354
Paczynski, B., Stanek, K. Z., Udalski, A., Szymanski, M., Kaluzny, J., Kubiak, M., Mateo, M., & Krzeminski, W. 1994, ApJ, 435, L113
Papayannopoulos, T., & Petrou, M. 1983, A&A, 119, 21
Piner, B. G., Stone, J. M., & Teuben, P. J. 1995, ApJ, 449, 508
Raha, N., Sellwood, J. A., James, R. A., & Kahn, F. D. 1991, Nature, 352, 411
Sandage, A. 1961, The Hubble Atlas of Galaxies (Washington: Carnegie Inst.)
Sanders, R. H., & Prendergast, K. H. 1974, ApJ, 188, 489
Schwarz, M. P. 1981, ApJ, 247, 77
———. 1984, MNRAS, 209, 93

Stanek, K. Z., Udalski, A., Szymanski, M., Kaluzny, J., Kubiak, M., Mateo, M., & Krzeminski, W. 1997, ApJ, 477, 163
Teuben, P., & Sanders, R. H. 1985, MNRAS, 201, 303
Teuben, P. J., Sanders, R. H., Atherton, P. D., & van Albada, G. D. 1986, MNRAS, 221, 1
Toomre, A. 1963, ApJ, 138, 385

van Albada, G. D. 1985, A&A, 142, 491
van Albada, G. D., & Roberts, W. W. 1981, ApJ, 246, 740
van Albada, G. D., van Leer, B., & Roberts, W. W. 1982, A&A, 108, 76
Wada, K., Taniguchi, Y., Habe, A., & Hasegawa, T. 1994, ApJ, 437, L123
Weinberg, M. D. 1992, ApJ, 384, 81
Zhao, H. S., Spergel, D. N., & Rich, R. M. 1994, AJ, 108, 2154